FRACTURE INITIATING MECHANISM IN ADDITIVELY MANUFACTURED 17-4 STAINLESS STEEL

A Thesis
Submitted to the Graduate Faculty
of the
North Dakota State University
of Agriculture and Applied Science

By

Anik Das Anto

In Partial Fulfillment of the Requirements
for the Degree of
MASTER OF SCIENCE

Major Department:
Civil, Construction & Environmental Engineering

November 2022

Fargo, North Dakota

North Dakota State University
Graduate School

Title

FRACTURE INITIATING MECHANISM IN ADDITIVELY MANUFACTURED 17-4 STAINLESS STEEL

By

Anik Das Anto

The Supervisory Committee certifies that this ***disquisition*** complies with North Dakota State University's regulations and meets the accepted standards for the degree of

MASTER OF SCIENCE

SUPERVISORY COMMITTEE:

Ravi Kiran Yellavajjala
Chair

Mijia Yang

Chad Ulven

Approved:

11/17/2022
Date

Xuefeng (Micheal) Chu
Department Chair

ABSTRACT

Additive manufacturing provides exceptional geometrical freedom to the designers and enables the production of parts that cannot be made through subtractive processes. Defects in additively manufactured (AM) metals are detrimental to the manufactured components. This study aims to understand the fracture initiation mechanism in as-built AM 17-4 stainless steel. Micro-computed tomography (micro-CT) analysis was conducted on the undeformed and fractured unnotched and notched specimens to characterize the defects in the as-printed specimens before and after deformation. The micro-CT analysis showed that the initial void count and volume fraction increased after the deformation indicating new void nucleation and dilation of voids. Furthermore, coalesced void colonies were noticed in the fractured specimens in the vicinity of the fracture surface. Evidence for void nucleation, dilation, and coalescence indicates ductile fracture to be the fracture initiation mechanism in AM 17-4 steel.

ACKNOWLEDGEMENTS

I would like to express my sincere gratitude and thanks to my advisor Dr. Ravi Kiran Yellavajjala for his constant support and guidance throughout this journey at NDSU. I am also very thankful to my committee members Dr. Mijia Yang and Dr. Chad Ulven for generously offering their precious time.

I am particularly grateful to Dr. Scott Payne, and Jayma Moore of the Electron Microscopy Center at NDSU for their help to conduct micro-CT and SEM analysis. I would like to extend my gratitude to Rob Sailor of Mechanical Engineering for helping me to conduct fracture tests. Additionally, I would like to thank Hizb Ullah Sajid for modeling and printing the AM specimens. I would also like to thank all the members of Damage in Materials and Structure (DAMS) Research Group, particularly Surajit Dey, for their support and help.

I am very thankful to my family for their endless encouragement, love, and support throughout my life.

TABLE OF CONTENTS

LIST OF TABLES

LIST OF FIGURES

LIST OF ABBREVIATIONS

CAD .....Computer-Aided Design.

EBM .....Electron Beam Melting.

LPBF .....Laser Powder Bed Fusion.

SLM .....Selective Laser Melting.

SLS.....Selective Laser Sintering.

DMLS .....Direct Metal Laser Sintering.

LEAP.....Leading Edge Aviation Propulsion.

DMAM.....Direct Metal Additive Manufacturing.

LOX .....NASA Liquid Oxygen.

AM .....Additively Manufactured.

LOF .....Lack of Fusion.

HIP .....Hot-Isostatic Press.

TIP.....Thermally Induced Porosity.

GTN .....Gurson-Tvergaad-Needleman.

Micro-CT .....Micro-computed tomography.

SEM .....Scanning Electron Microscopy.

RU .....Reference Unnotched.

CN .....C-notched.

FEA .....Finite Element Analysis.

EBSD .....Electron Backscatter Diffraction.

OM .....Optical Microscope.

EM.....Electron Microscope.

CCD .....Charged-Coupled Device.

EBSD .....Electron Backscatter Diffraction.

LIST OF SYMBOLS

$\bar{x}^*$ .....The natural logarithmic mean of the random variable.

s^* .....The natural logarithmic standard deviation of the random variable.

$\bar{x}$ .....The mean of the random variable.

s .....The standard deviation of the random variable.

1. INTRODUCTION

1.1. Background

Additive manufacturing is a technique used to fabricate three-dimensional objects layer-by-layer from powder, wire, or sheets using three-dimensional computer-aided design (CAD) model data without any secondary processing [1]. The main advantage of additive manufacturing over the conventional subtractive fabrication and shaping process is that it can quickly produce complex parts with optimized geometry and functionality in relatively small production units [2]. Moreover, unlike conventional subtractive manufacturing, the additive manufacturing process does not involve the discharge of wastes which aids in maintaining sustainability by repairing, remanufacturing, extending lifetime, recycling, consolidating parts, and optimizing processes to save energy and material that promotes green technology [3]. Different metallic alloys such as-stainless steel, aluminum alloys, titanium alloys, copper alloys, super alloys, cobalt alloys, and refractory alloys are employed in powder or wire form depending on the additive manufacturing process [1,4–6]. Metal additive manufacturing is often differentiated into two broad categories based on feedstock: (i) powder bed system and (ii) powder or wire feed system [1,4]. Powder bed systems can be classified in terms of the source of the powder into two categories: electron beam melting (EBM) and laser powder bed fusion (LPBF). LPBF technique can be classified as selective laser melting (SLM), selective laser sintering (SLS), and direct metal laser sintering (DMLS) [1,4,7]. LPBF is becoming popular for manufacturing metallic parts with complex geometry. In the LPBF procedure, thin layers of powder are deposited on the build plate, and the laser beam is implemented as a power source to fuse the powders at the locations according to the pre-defined line pattern extracted from CAD model geometry to fill the 2D layer of the part [8]. A new layer of powder is applied when one layer is completed, and the process is repeated

until the 3d part is manufactured. The powder delivery system comprises a platform to supply powder, a roller to distribute powder to create the layer of powder, and another platform to hold the manufactured component (see Figure 1). A laser and a scanner with optics are used as an energy delivery system, which helps to deliver focused spots to all points of the build platform. A flow of gas (argon or nitrogen) is flowed over the powder bed to provide protection of the manufactured part against oxygen and clear the metal fumes and spatter generated from the laser path [9].

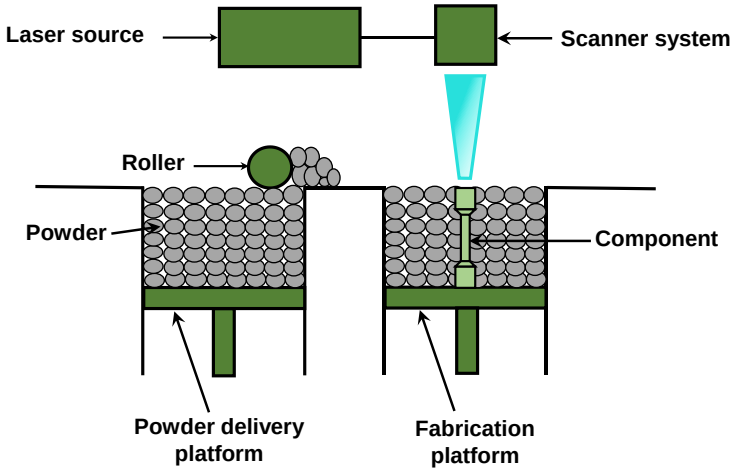

Figure 1. Schematic diagram of the laser powder bed fusion (LPBF) additive manufacturing process.

In the aerospace industry, metal additive manufacturing amalgamates multiple components to enhance performance within timeline and economic constraints, better risk management, and shape complex geometry to enable mass lightening [10]. Due to the advent of additive manufacturing, the intricate parts of aircraft such as, cooling channels in turbine blades [11], aircraft oil coolers [12], and liquid rocket engine thrust chambers [13], which were difficult and time-cumbersome to manufacture previously, became more accessible. Recently, the nozzle of a leading edge aviation propulsion (LEAP) jet engine, developed by General Electric and Snecma, was redesigned with a single part and reduced number of welded or brazed joints by

applying direct metal additive manufacturing (DMAM) [14]. A320 nacelle hinge bracket [15], rocket engine injectors by NASA [16], and the stator of a NASA liquid oxygen (LOX) turbopump [16] are a few more examples of the components of aircraft and spacecraft that are commercially produced using metal additive manufacturing. . Furthermore, metal additive manufacturing ensures clean and efficient energy production with reduced greenhouse gas emissions and pollution with its application in the fabrication of parts and core components required for the production and storage of energy [17]. For instance, Westinghouse utilizes powder-bed fusion to additively manufacture reactor components of its nuclear energy plants made of 316L stainless steel, Zirconium alloys, and Inconel 718 [17]. In addition, three-dimensional printed bottom nozzle for debris-filtering in the nuclear fuel assembly [17], fabrication of electrodes of a micro-battery [18], synthesis of membrane and anode components of a microbial fuel cell [19], and manufacturing of Masoneilan control valve parts with unique configurations using metal laser sintering by General Electric Oil and Gas [17] are few of the applications of metal additive manufacturing in the energy sector. Different metals, such as stainless steel, magnesium, Co-Cr alloy, and Ti alloys, are used as raw materials for additively manufactured (AM) biomedical products [20].

Even though the applications and uses of metal additive manufacturing are rapidly growing, failures and damages are common in AM metal parts and components due to manufacturing defects or flaws [21]. More precisely, failure occurring in the service stage can be attributed to the shortcomings of the design and fabrication processing stages. The localized heating and rapid cooling with powdered feedstock act as a favorable environment for forming small cracks, unmelted particles, gas bubbles, and a lack of fusion regions during manufacturing [22]. More specifically, defects from design, fabrication processing, and service stages are

mainly responsible for the fracture and failure in AM metals [23]. Firstly, poor design choice results in a rough surface finish, residual stress gradient, microstructure with elongated grains, lack of fusion porosity, and gas porosity, leading to fracture [24]. Poor design choice includes the wrong selection of metal additive manufacturing process, materials, or parts to be produced using the metal additive manufacturing technique or combination of all three without considering the metallurgical characteristics and the load distribution within the manufactured hardware [23]. Secondly, several internal and surface defects are responsible for fracture initiation during the metal additive manufacturing process [23]. The surface defects result from keyholing, balling, warping or curling, craters, ejected molten droplets, swelling from melt pool, unfused powder, unmelted or partially melted powder particles, weld tracks, lack of fusion, and roughness [1,25]. Finally, these internal and external defects can also initiate fracture during service [26].

In the metal additive manufacturing technique, defects can be classified into three subgroups such as: (i) powder-related defects, (ii) fabrication processing-related defects, and (ii) post-processing-related defects [27]. The primary sources of powder-related defects are powder characteristics, surface contamination, and trapped gas [27]. Effects defects due to powder on the surface roughness, porosity, density, and mechanical properties in the AM components were studied in the past [7,28]. Without optimized process parameters such as laser power, layer thickness, hatch spacing, and scan speed can generate defects, including a lack of fusion (LOF) voids and keyhole pores [27,29,30]. Supply of optimized energy to the melt pool is necessary to melt the previously deposited layer and to ensure perfect bonding between layers. Lack of optimized energy supply to the melt pool may result in inadequate melting, vaporization, poor bonding, and LOF defects. The defects have sharp edges and are elongated between the layers [31,32]. Moreover, excessive energy and low scanning speed to the melt pool will result in

substantial vapor recoil forces and damaging convection currents, leading to spherical voids and gas bubbles due to the surface tension of the melt pool [8]. It is challenging to remove gas pores by post-processing and depends on the solubility of the contaminated gas [33]. At the time of re-melting during the deposition of the next layer, the gas bubble formed on top of the melt pool escapes to the gas bubble deeper in the melt pool, which generates keyhole-induced more detrimental porosity [34]. Post-processing techniques such as heat and hot-isostatic press (HIP) treatment usually reduce inherent defects [35,36]. However, inert gas in the HIP chamber can help regrow thermally induced porosity (TIP) [37]. Thus the characterization of the defects in the AM components is necessary for as-built and post-treated conditions.

The optical microscopy and scanning electron microscopy (SEM) are most commonly used techniques for inspecting the microstructure of materials by two-dimensional imaging. However, the microscopes only provide information about specific sections of the sample that does not represent the whole part's structure with non-homogeneously distributed defects. Sanaei et al. [30] employed the optical microscope and scanning electron miroscope to evaluate the surface roughness of AM Ti-6Al-4V samples. The density-based two methods: the Archimedes method and gas pycnometry, are unsuitable for quantitatively determining defects' size, shape, location, or distribution as these methods are only suitable for small volume parts [38]. The potentially non-destructive strategy, micro-computed tomography (micro-CT), is more appropriate for investigating the internal structure and controlling the quality of metals [39]. Solberg et al. [40] employed X-ray computed tomography to visualize the unfavorable distribution of significant defects and the defects' size, similar to the defects found to initiate failure from fractography. Gong et al. [41] utilized micro-CT to locate the internal defect structure involving porosity and inclusions of Ti-6Al-4V rectangular samples made by SLM and

EBM. Defect characteristics and their variability were studied using micro-CT analysis by Sanaei et al. [30], and the defects have irregular shapes with much less sphericity. The effect of the internal pores on the tensile behavior of AM 316L steel were investigated using X-ray computed tomography by Wilson-Heid et al. [42]. The intentional and unintentional pores in the AM components can initiate early fracture [42,43].

Fractures observed in metals can be classified into three categories such as, (iii) ductile fracture, (i) transgranular cleavage fracture, and (ii) intergranular fracture. Ductile fracture, also known as fibrous or dimpled fracture, is a common fracture initiating mechanism in metallic materials with significant plastic strain. Ductile fracture is a multi-step process that starts with the nucleation of voids from the inclusions, and those nucleated voids grow with the aid of plastic strain (see). Eventually, the ductile failure can be triggered by the coalescence of the voids or shear localization due to plastic instability. A ductile fracture can be characterized by the presence of microscopic microvoids in the fracture surface of the specimens. Transgranular fracture is a brittle type of fracture which occurs due to the separation of the material along the atomic planes. The formation of the rivers-like pattern is observed in the specimens' fracture surface. Intergranular fracture is a rare type of brittle fracture that occurs along the grain boundaries of the metals. Intergranular fracture is a type of brittle fracture which is caused due to segregation of impurities at the grain boundaries [44]. This results in weakened grain boundaries and facilitates crack propagation along the grain boundaries. Grain boundaries are visible in the fracture surface in the intergranular fracture. Different types of fractures in conventional metallic materials have been well-defined experimentally and computationally [44,45]. Thus, the fracture behavior of AM metals gets a lot of attention.

A modified Gurson-Tvergaad-Needleman (GTN) model was adopted by Yang et al. [46] to predict the ductile fracture behavior of the AM Ti6Al4V alloy. The authors proposed an inverse analysis technique to calibrate the modified GTN parameters. Another study by Muro-Barrios et al. [47] presented a dual-scale porosity failure process for the AM Ti6Al4V alloy where they proposed a computational cell model based on Gurson porous material model and characterized the defects using optical and electron microscopy. Nalli et al. [48] calibrated the parameters of uncoupled ductile fracture models for AM Ti6Al4V, 17-4 PH and AlSi10Mg alloys. Naragani et al. [49] determined the grain-scale description of void growth and coalescence in AM IN718 alloy. Kim et al. [50] investigated the effect of an artificial internal defect on tensile loading by introducing a octahedral defect by changing the process parameter in LPBF 17-4 steel. Miers et al. [51] evaluated effect of porosity on the stain localization in LPBF 316L stainless steel. These studies cannot explain the nucleation of new voids, the inherent defects' growth, and the voids' coalescence in the AM metals. Though few researchers have attempted to explain the ductile fracture in AM metals, understanding the fracture in AM steels needs more community efforts.

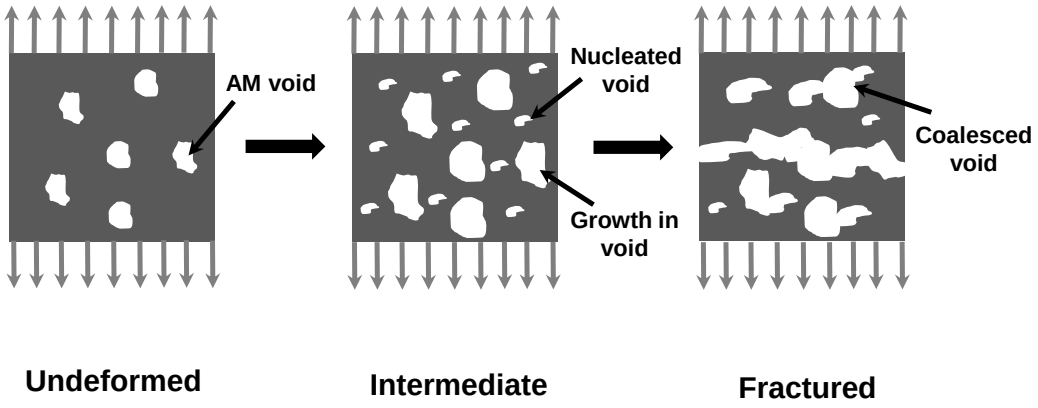

Figure 2. Ductile fracture process in metals.

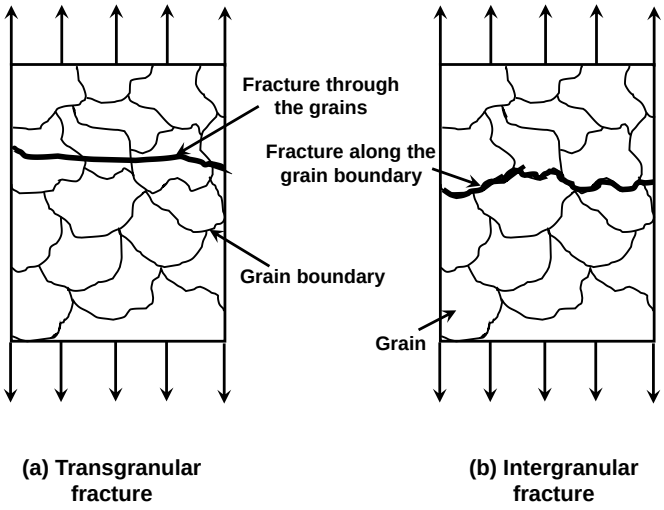

Figure 3. (a) Transgranular cleavage fracture and (b) intergranular fracture in metals.

1.2. Research Gaps

Defects in as-built AM steel may lead to early fracture due to reduced strength and ductility [4,42]. The fracture initiating mechanism in the as-built AM 17-4 stainless steel is still elusive to the additive manufacturing community. There is also a lack of research works in identifying the influence of AM defects on the fracture initiation in as-built AM 17-4 stainless steel. Therefore, to understand the influence of AM defects on fracture, we need to quantitatively characterize the defect distribution in the as-built AM steel test specimens before and after fracture. Furthermore, the effect of geometrical complexities or intricacies on AM defects remains unexplored, and their influence on the fracture initiation is yet to be investigated.

1.3. Research Objectives

This study aims to investigate the fracture initiating mechanism in AM steel using SEM and micro-CT. The objectives of this study are as follows:

(i) to quantify the growth of the number of voids and void volume in AM specimens after deformation.

(ii) to determine the statistical distribution of void features of AM steels before and after deformation.

(iii) to investigate the influence of sudden geometrical changes on the size and density of AM defects.

(iv) to elucidate the fracture initiating mechanism and evaluate the characteristic length over which the voids have to grow to initiate fracture.

1.4. Organization of Thesis

The thesis is organized as follows:

Chapter 2: Materials and Methods: The materials, additive manufacturing technique, processing parameters, geometry, tensile testing process, and finite element modeling are presented. The characterization techniques of the defects in the AM steels are also illustrated in this chapter.

Chapter 3: Results and Discussion: In this chapter, the statistical distribution of the voids in AM steels are investigated through the analysis of micro-CT data. Based on this analysis, the voids' nucleation, growth, and coalescence are identified. Finally, the fracture initiating mechanism is explained, and the characteristic size of the void is determined.

Chapter 4: Conclusions and Future Work: Conclusions based on chapter 3 are presented. Future work related to the post-treatment to reduce the inherent defects in AM steels and computational modeling of AM steel fracture is also provided in this chapter.

2. MATERIALS AND METHODS

2.1. Additive Manufacturing Process Parameters and 17-4 Steels

The specimens used in the present study were additively manufactured employing DMLS from 17-4 stainless steel spherical powder with a particle diameter of 36-44 µm. 17-4 stainless steel specimens were printed with the following process parameters: laser power of 220 W, 70 µm laser beam diameter, scanning speed of 755 mm/s, and a 0.11mm hatching space. A 90° build orientation with the build plate and a layer thickness of 40 µm are used as build parameters. The present study aims to understand the deformation behavior and failure initiating mechanism in the as-printed AM steel specimens. Therefore, post-processing heat treatment was avoided for the steel test specimens which is usually employed to reduce the material defects in AM specimens. A similar study on understanding the fracture behavior of heat-treated 17-4 PH stainless steel specimens will be conducted in the future.

17-4 stainless steel was used in the present study due to its wide range of engineering applications. 17-4 stainless steel finds its application in aerospace [52], surgical instrumentation [53], naval [54], nuclear [55], and petrochemical industries [56] due to its high strength, fracture toughness, hardness, and excellent corrosion resistance [52–56]. The material properties of 17-4 stainless steel can be partly attributed to the chemical composition of the steel powder which is presented in Table 1. 17-4 stainless steel powder comprises of 15-17.5 wt.% chromium, 3-5 wt.% nickel, and 3-5 wt.% copper which combinedly provide high corrosive resistance and conductivity [57,58]. The microstructure of 17-4 stainless steel was studied in the laboaratory using small disc-shaped specimens which were grinded using silicon carbide (SiC) paper with grit size in the following order: 60, 120, 400, 800, and 1200. Furthermore, the grinded steel specimens were polished using alumina suspension and were subsequently etched using Fry's

reagent. Finally, the etched steel specimens were observed under a light microscope. The melt pool boundaries, layer thickness, and hatch spacing are clearly visible in the optical micrograph (see Figure 4). Moreover, the microstructure is also responsible for the material's favorable mechanical properties, and microstructural characterization is discussed in the following section.

Table 1. Chemical composition of 17-4 stainless steel powder.

Element	Wt (%)
C	Max. 0.07
Cr	15-17.5
Cu	3-5
Mn	Max. 1.0
Nb	0.15-0.45
P	Max. 0.04
S	Max. 0.03
Si	Max. 1.0
Ni	3-5
Ta	0.15-0.45
Fe	Balance

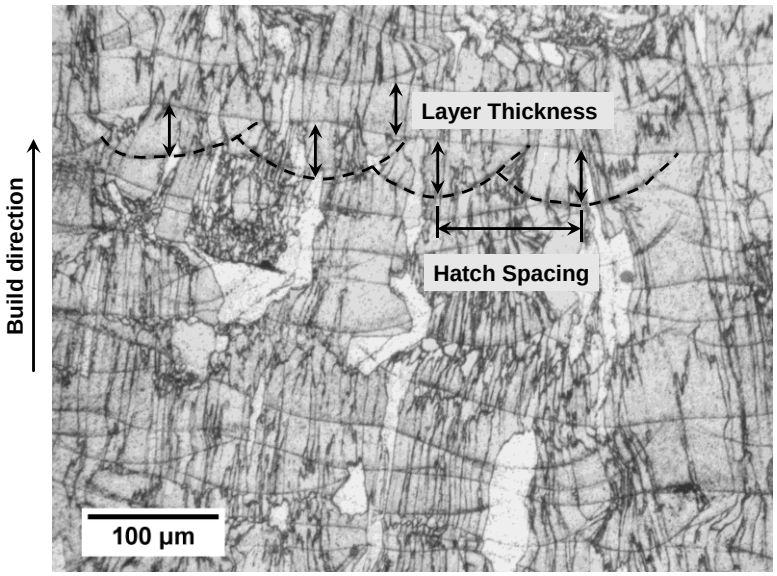

Figure 4. Optical micrograph of the 17-4 AM stainless steel parallel to the build direction.

2.2. Geometry of the Specimens and FE Analysis

In this study, one reference unnotched (RU) and C-notched (CN) axisymmetric cylindrical specimens were considered. Three different notch radii (CN1: 0.5 mm, CN2: 1 mm, and CN3: 1.5 mm) were used to achieve a wide range of stress triaxialities and to understand the response of the material when subjected to a sudden change in geometry in the critical section. Furthermore, these specimens were also used to study the AM defects near geometrical discontinuities. The geometric details and dimensions of the AM 17-4 stainless steel specimens are provided in Figure 5. Uniaxial tension tests were performed using a servo-hydraulic MTS 809 load frame. A uniform displacement rate of 0.02mm/s was maintained during the uniaxial tension tests. The elongation of the deformed test specimens was monitored using a contact extensometer with 1-inch (25.4 mm) gauge length (Epsilon model 3542). The engineering stress strainload curves obtained for various test specimens are shown in

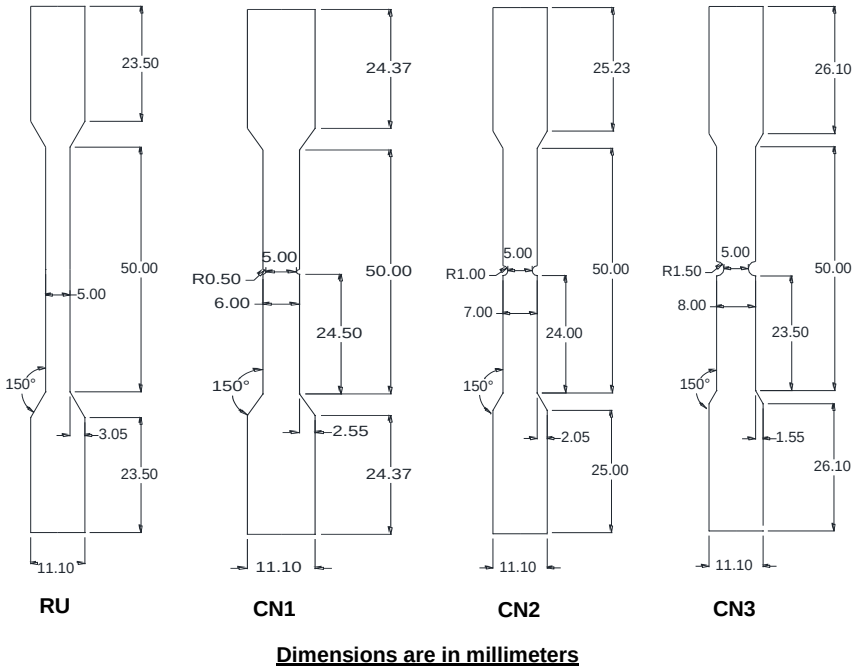

Figure 5. Geometric details of test specimens. RU(referenced unnotched), CN(circular notched).

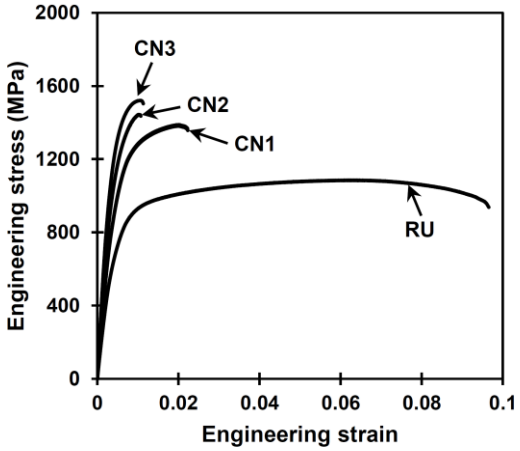

Figure 6. Experimental engineering stress-strain curves of the AM test specimens.

Finite element analysis (FEA) was conducted using the commercially available FEA package ABAQUS® for both unnotched and notched test specimens. The finite element models were discretized using four noded bilinear axisymmetric CAX4 elements available in the ABAQUS® library. J_2 plasticity constitutive model was used to capture the material non-linearity, and a non-linear geometric solver was used to obtain the finite element solutions. The strain hardening curve for the J_2 plasticity model was obtained from the experimental stress-strain curve of the reference unnotched specimen and the Ramberg–Osgood relationship (see Figure 7a). The boundary conditions used for the finite element models are shown in Figure 8. The engineering stress-strain curve obtained from FEA was compared with the experimental stress-strain curve to validate the finite element model (see Figure 7b). The stress triaxiality and equivalent plastic strain distributions across the critical section (least cross-section) of the test specimens at fracture were extracted from the non-linear finite element analysis and are presented in Figure 9 and Figure 10, respectively. The maximum stress triaxiality across the critical cross-section of the steel specimens at fracture ranged from 0.3 to 1.13. Equivalent plastic strains have higher values in the vicinity of the notches in the notched specimens.

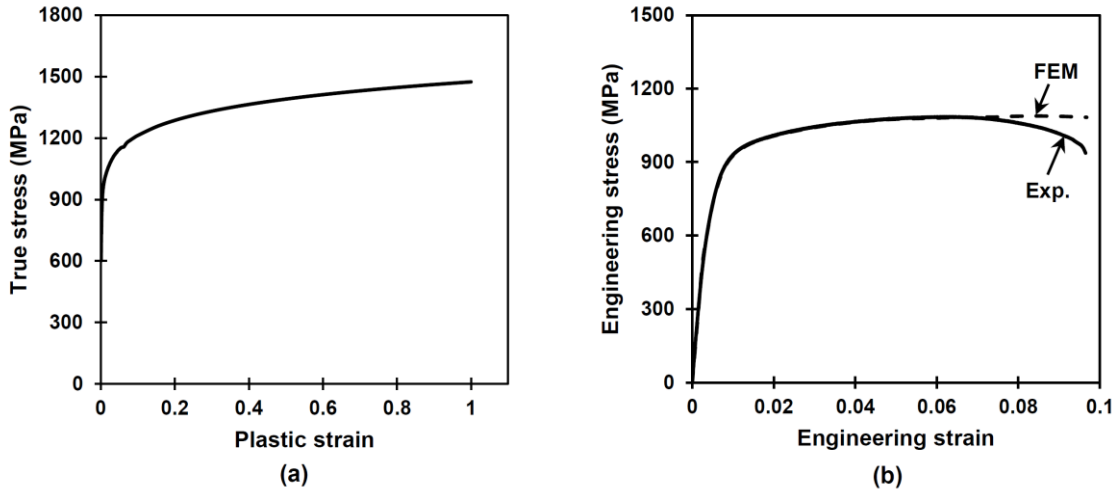

Figure 7. (a) Strain hardening curve of reference unnotched AM 17-4 steel specimen, (b) experimental and FEM engineering stress-strain curves of reference unnotched specimen.

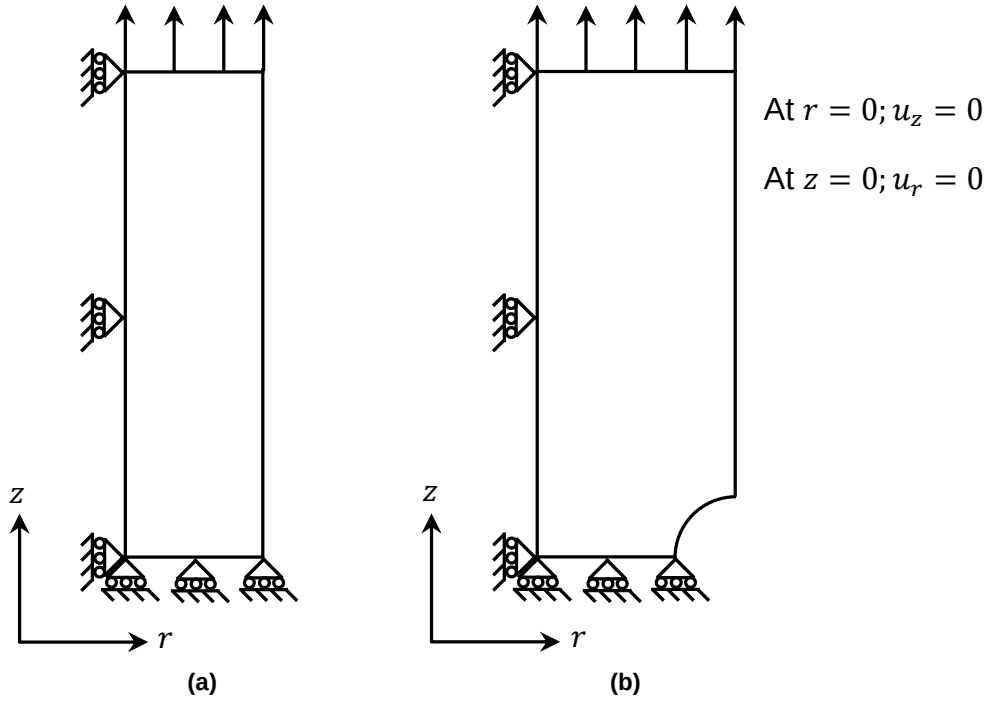

Figure 8. Applied boundary conditions. (a) referenced unnotched (RU) specimen, (b) notched specimen.

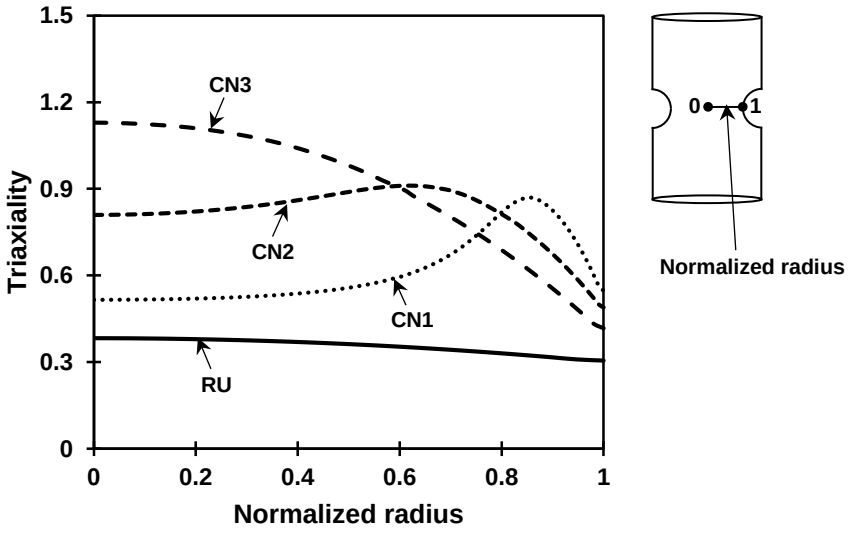

Figure 9. Triaxiality profiles at fracture for as-built AM 17-4 stainless steel specimens.

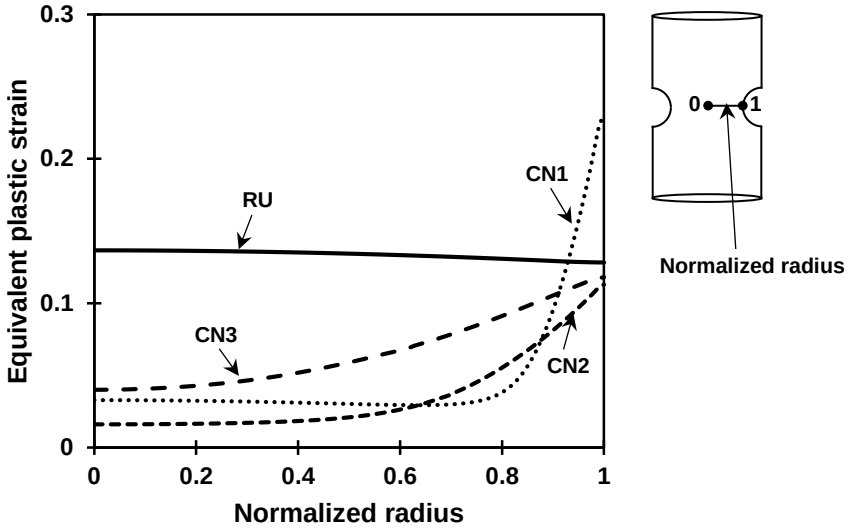

Figure 10. Equivalent plastic strain profiles at fracture for as-built AM 17-4 stainless steel specimens.

2.3. Microstructure Characterization

The fracture initiation mechanism for rolled 17-4 steel has been studied [59–61]. The wrought 17-4 steel microstructure contains a martensitic structure, whereas the AM 17-4 steel is δ-ferritic with elongated columnar grains along the build direction [61]. However, this study has

quantified the distinct microstructure of AM 17-4 steel by employing Electron Backscatter Diffraction (EBSD). EBSD is a scanning SEM based technique with a diffractor that reveals crystallographic details such as phase, texture or crystallographic orientations, grain size, grain shape, and average grain orientation [62]. The samples of EBSD analysis must be prepared by carrying out several steps: sectioning, grinding, polishing, and etching using the standard EBSD sample preparation technique [35]. The samples were mounted in 1 inch epoxy rounds. These were then ground on SiC papers, starting at 240 grit then using 320, 400, 600, and 1200 grit at 200 rpm. After this, the samples were diamond polished for 10 minutes each on 6 µm, 3 µm, and 1 µm. Final polishing using 50nm colloidal silica polish was performed for 30 minutes. Once polished, the samples were coated with 5nm of Carbon to maintain conductivity in the SEM. EBSD analysis was performed using JEOL 6500 SEM integrated with an EBSD system to investigate the grain morphology and crystallographic orientations. The following settings were maintained for the EBSD investigation: 20 nA of beam current, 20 kV of accelerating voltage, 70° specimen tilt angle, 78.66% hit rate, and an acquisition speed of 1399.76 Hz. The band contrast microstructure of the 17-4 AM stainless steel, analyzed using the SEM, is illustrated in Figure 11. The grain size of AM steel is larger than that of wrought steel, and the grain structure of AM steel is not as equiaxed as wrought steel. The martensitic structure can provide maximum hardness, and the ferritic structure is soft and ductile. So, crack initiation and growth are easier in ferritic AM steel than in martensitic wrought steel [61]. EBSD orientation maps and FCC/BCC phases for the horizontal and vertical cross-sections are shown in Figure 12. There is a significant difference in grain orientation and grain size of the horizontal and vertical sections of the AM 17-4 stainless steel test specimens. The average length of the grains in the horizontal and vertical cross-sections are 3.38 µm and 4.07 µm, respectively. Equiaxed and columnar grains

were identified in both the horizontal and vertical sections as shown in Figure 11. The horizontal section of the test specimen is dominated by equiaxed grains, whereas elongated columnar grains are primarily identified in the molten pool boundaries of the vertical section. The maximum aspect ratio ranges from 1.06 to 8.12 and 1.06 to 15.03 for the horizontal and vertical sections, respectively. The EBSD analysis also indicates that the 17-4 stainless microstructure is largely dominated by the BCC/BCT phases compared to that of the FCC phase, which is consistent with the literature [35,61]. The presence of the ferritic phase in the AM 17-4 stainless steel could provide high ductility, but inherent defects in the as-built AM components lead to early failure. Thus, a comprehensive study of the fracture initiation mechanism is presented in the following sections.

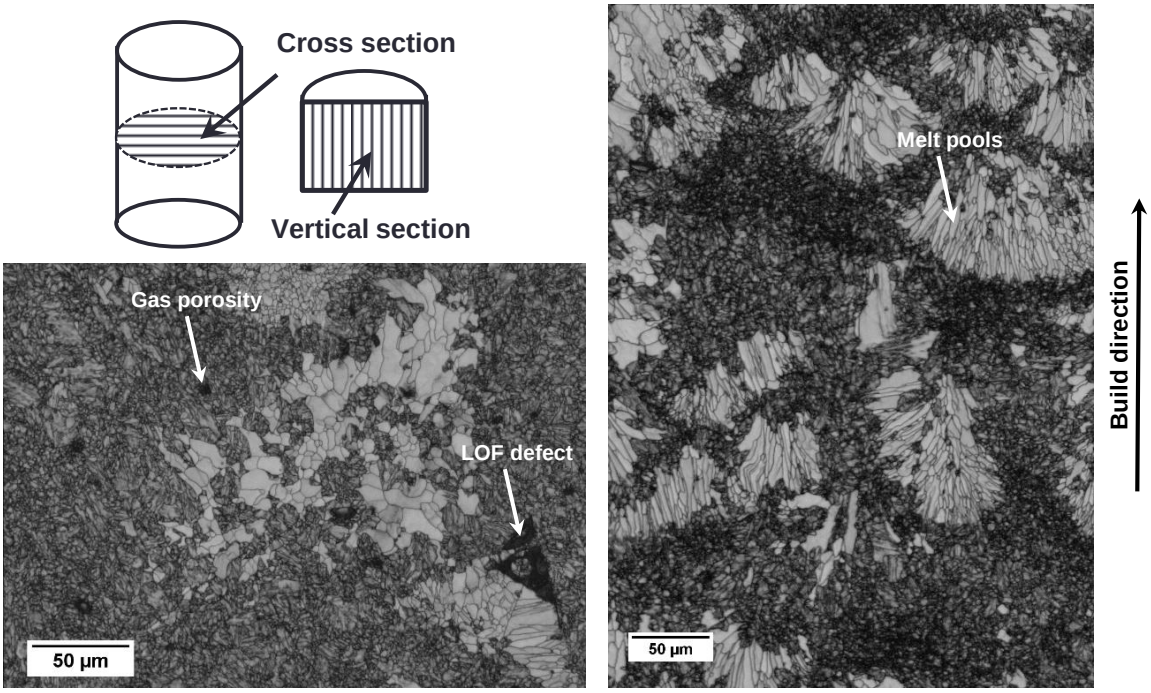

Figure 11. SEM microstructures of the 17-4 AM stainless steel (a) cross-section (perpendicular to the build direction) and (b) vertical section (parallel to the build direction).

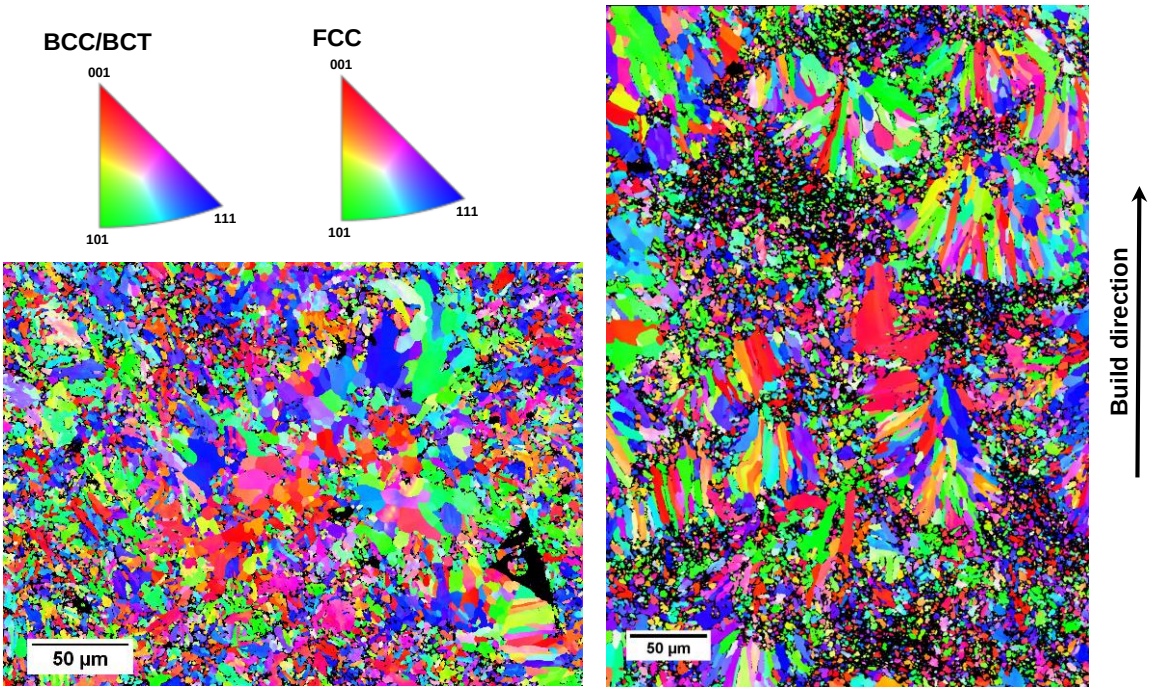

Figure 12. EBSD orientation maps of the 17-4 AM stainless steel specimen. (a) cross-section (perpendicular to the build direction) and (b) vertical section (parallel to the build direction). The IPF triangles apply to both sections.

2.4. Void Characterization and Quantification

2.4.1. Techniques for Void Characterization

2.4.1.1. SEM

The optical microscope (OM) and electron microscope (EM) have the same working principle and are used for surface characterization. However, the source of OM is visible light, and the source of EM is the focused accelerated electron beam. EM provides higher resolution data than OM as electrons have a shorter wavelength and are more energetic than visible light [63]. SEM is an advanced universal instrument widely implemented to visualize the surface of materials with a spatial resolution of 1 nm and provide information about the topography, shape, size, texture, composition, orientation of grains, and crystallography [64]. The specimen is stuck on the stage by the double-sided carbon tap to get good imaging. First, primary electrons are

emitted from the electron gun, and the electrons move through the condenser and objective lenses and generate an electron beam of a few nanometers in diameter. Then electron signals are generated when the electron beam interacts with the specimen surface for scanning over the surface [65]. This specimen and electron beam interaction generates different electron signals, such as Auger electrons, characteristic x-rays, transmission electrons, absorption electrons, backscattered electrons, and secondary electrons [65,66]. The detector detects the electron signals, transforms the amount of the detected electrons into the brightness of the corresponding points, and forms the corresponding electron image to display on a screen [65]. However, SEM images attain information about the surface of the specimen, and the internal structure remains concealed.

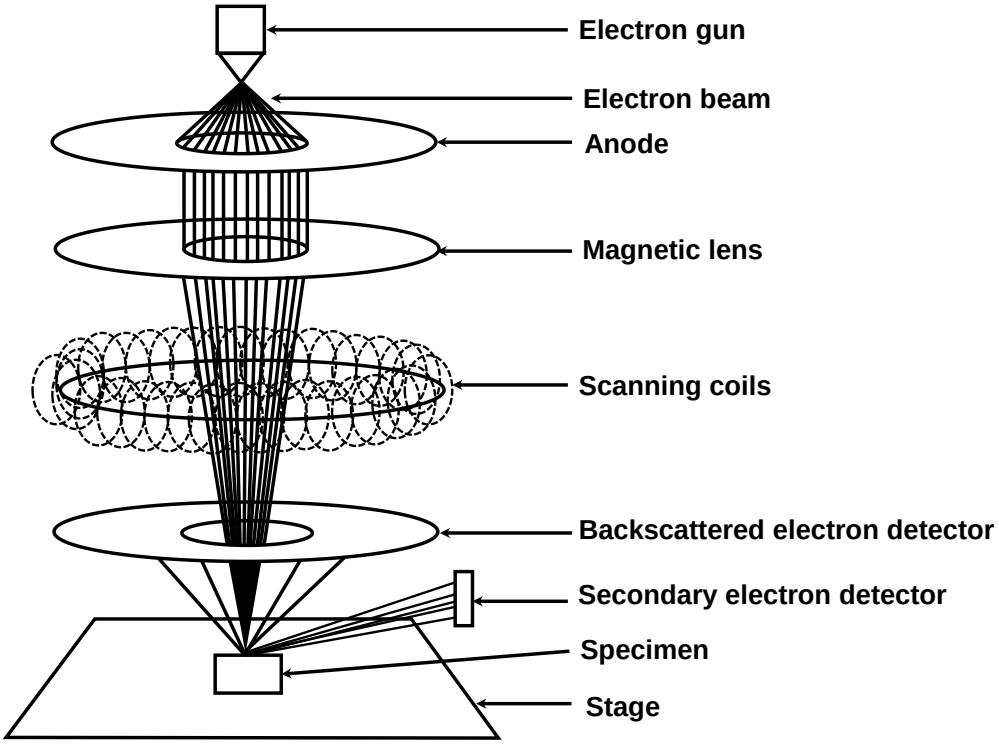

Figure 13. Schematic diagram of a scanning electron microscope.

2.4.1.2. Micro-CT

Micro-CT is advanced instrumentation through which the internal 3D structure of a material can be reconstructed through the different X-ray attenuation of materials. Micro-CT comprises an X-ray tube that emits X-ray, a sample holder, a detector, and a video camera with a high-resolution charged-coupled device (CCD). The generated X-ray passes through the sample and forms a shadow projection on the detector or CCD camera. The CCD camera cannot detect the X-ray, so the scintillator converts the X-rays into visible light, and then the CCD camera can detect the projection. The sample holder, the detector, or the X-ray source rotates (180° or 360°) to capture the shadow projection of different orientations [67,68]. The back projection algorithm is employed to reconstruct the 2D structure to the 3D structure [69]. The reconstructed 3D structure is then analyzed using an image processing algorithm[68].

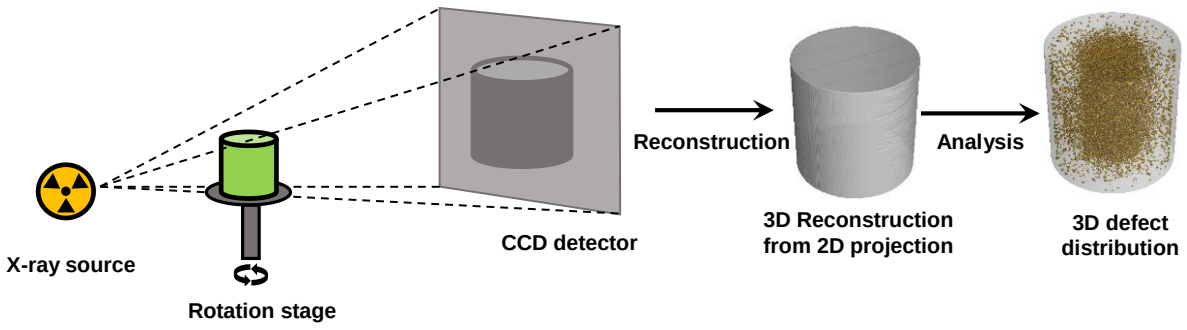

Figure 14. Schematic diagram of a typical micro-CT scan and reconstruction.

2.4.2. Investigation of Fracture Type Employing SEM

SEM analysis of the fracture surfaces of the AM 17-4 stainless steel test specimens was conducted to decipher the microscopic damage mechanism. The fractured samples were attached to cylindrical aluminum mounts with double-sided XYZ adhesive tape to view the fracture surface of the test specimens. The images of the fracture surfaces were obtained at an

accelerating voltage of 15kV using a JEOL JSM-6490LV SEM (JEOL USA, Peabody MA, USA). Typical SEM micrographs of the fracture surfaces of the reference unnotched (RU) and notched (CN1) test specimens are presented in Figure 15 and Figure 16, respectively. Furthermore, magnified images of five different locations on the fracture surface of the test specimens are also presented. The regions were divided based on varying stress and strain states across the cross-section of the test specimens, which was obtained using the finite element analysis discussed earlier. Fractures in steel can be classified into three categories: ductile fracture, intergranular fracture, and transgranular cleavage fracture. Ductile fracture in the steel originates from microvoid nucleation followed by growth of the voids and finally coalescence leading to fracture during plastic deformation [70,71]. The microvoids nucleate due to debonding and/or cracking of the secondary particles in the steel matrix. Other than the nucleated microvoids, material defects with an equivalent spherical diameter ranging from tens of microns to a few hundreds of microns (see Figure 11) are common in as-built AM steel specimens which can be attributed to gas porosity and lack of fusion defects [22,72]. These nucleated microvoids and/or existing material defects elongate and dilate due to the applied external load on the test specimen. Finally, these microvoids and/or defects coalesce to form cracks which initiate ductile fracture in the steel specimens [46]. Transgranular fracture is a brittle cleavage fracture characterized by river-like patterns and is caused due to the propagation of cracks through the grain interiors [44]. The SEM micrographs of the test specimens presented in Figure 15 and Figure 16 show majority of dimples with traces of river-like patterns on the fracture surface. Although small dimples with an average equivalent spherical diameter of ~1 μm are visible on the SEM fractographs, it is challenging to identify coalesced microvoid colonies on the fractographs of the test specimens responsible for ductile fracture in steel. The dimples' sizes are

more prominent in SEM fractographs of conventional 17-4 PH steel compared to AM specimens, and the coalesced void colonies can be identified on the fracture surfaces (see Figure 17). Therefore, the SEM study of fractographs of the AM 17-4 stainless steel specimens is insufficient in identifying the fracture initiation mechanism in the fractured steel specimens. Thus, a three-dimensional void identification technique needs to be adopted to elucidate the fracture initiation mechanism in AM 17-4 stainless steel specimens.

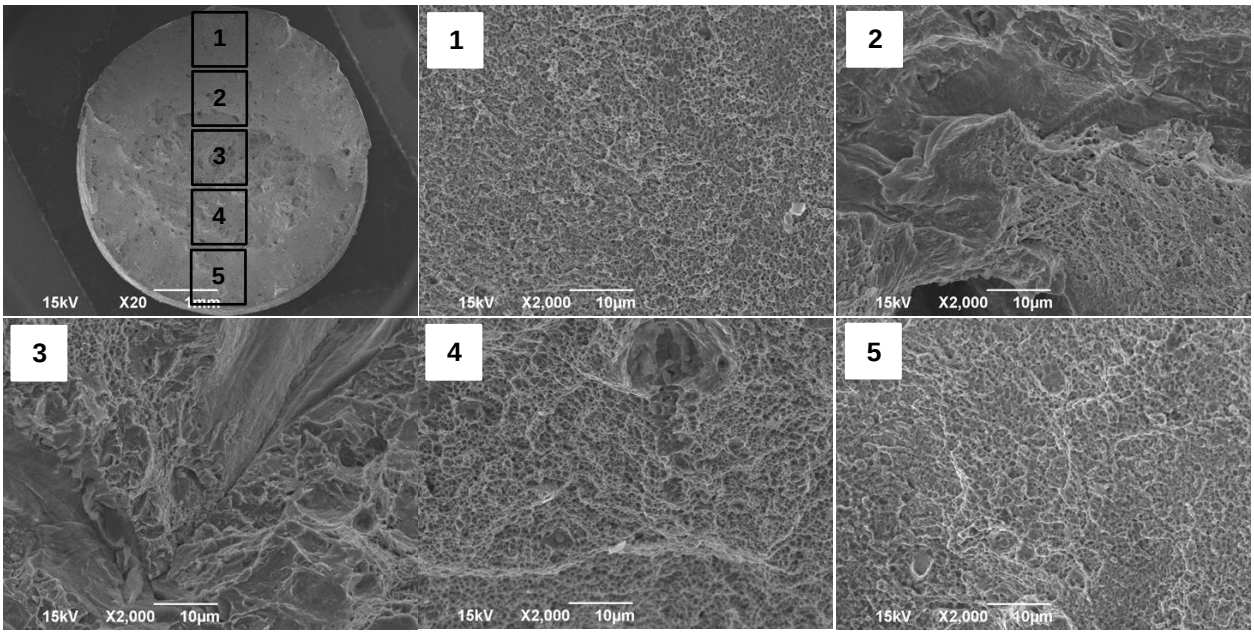

Figure 15. SEM analysis of the fracture surface of the AM unnotched 17-4 stainless steel specimen.

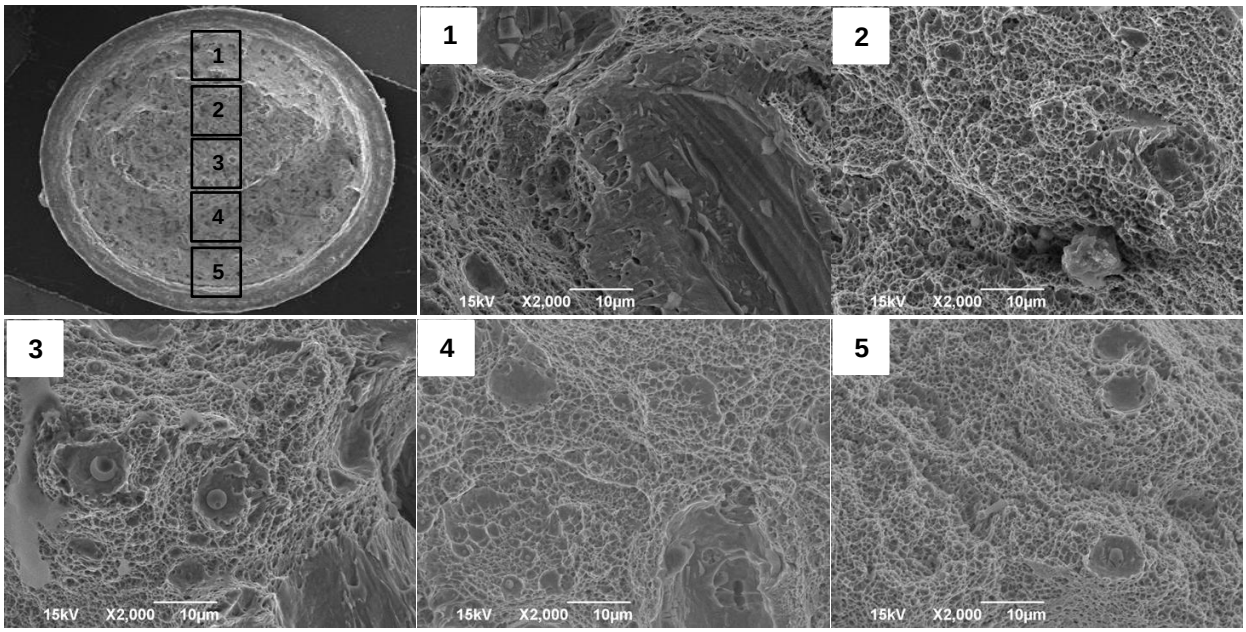

Figure 16. SEM analysis of the fracture surface of the AM notched 17-4 stainless steel specimen CN1 (notch radius 0.5 mm).

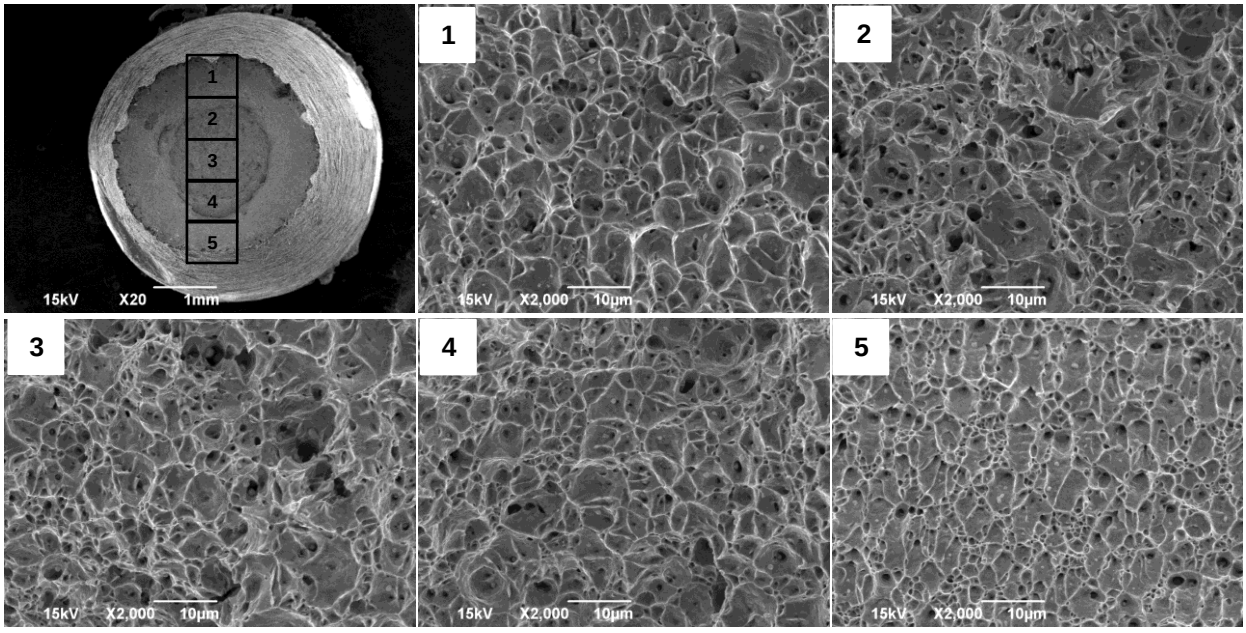

Figure 17. SEM analysis of the fracture surface of conventional unnotched 17-4 PH stainless steel specimen.

2.4.3. Micro-CT of AM Steel Test Specimens

The internal manufacturing defects in the AM steel specimens are difficult to detect using surface identification techniques. The defects in the as-built steel specimens considered in the

present study will be discussed in detail later in the section. Three-dimensional (3D) non-destructive techniques namely, Archimedes method and gas pycnometry may be used to identify internal defects in the test specimens; however, these methods are incapable of providing quantitative characteristics of the internal defects in the specimens [38]. Micro-CT is a 3D non-destructive technique initially developed for medical applications. Micro-CT is equipped with X-ray beams and detectors which extract images of a 3D object about an axis of rotation and reconstructs a 3D model of the object using algorithms [22]. Recently, Micro-CT has been introduced to AM metals for in-situ measurement of part geometry and defect characterization [22,38]. In the present study, micro-CT is used to characterize the manufacturing defects in the as-built AM steel test specimens, and the defect characteristics were utilized to understand the fracture initiating mechanism in the as-built steel specimens.

The micro-CT scans were conducted using GE Phoenix v|tome|x s X-ray computed tomography system equipped with a 180 kV nano focus X-ray tube and a high-contrast GE DXR250RT flat panel detector (GE Sensing & Inspection Technologies GmbH) at a voltage of 150 kV and a current of 350 µA with a diamond target. Detector timing ranged from 333-500 milliseconds, and 600-1000 projections were acquired. A voxel resolution of 16.9 µm was achieved during the scanning with a sample magnification of 11.835X. The acquired images were reconstructed into a volume data set using GE datos|x 3D computer tomography software version 2.8.0 RTM (GE Sensing & Inspection Technologies GmbH). A minimum of 8 voxels were considered a threshold for a single void to remove reconstruction artifacts and noise, resulting in a void volume of 38,608.4 μm^3 and equivalent spherical diameter of 41.93 µm. The minimum detectable void in the micro-CT scan is close to the layer thickness (40 µm) in the DMLS technique and the mean diameter of the particles (around 40 µm) used in additive

manufacturing the 17-4 stainless steel specimens. It will be possible to capture the common manufacturing defects in as-built AM components with this voxel resolution.

All the notched and unnotched AM 17-4 stainless steel specimens were subjected to micro-CT scans both before and after the fracture. The tensile test specimens were scanned over a distance of 15 mm from the center of the gauge length. The scanned section of each test specimen was further divided into three separate 5 mm zones: A, B, and C, for the evaluation of local characteristics of voids before and after deformation (see Figure 18). The number of zones is limited to three, so a sufficient number of defects are available in each zone for statistical analysis of the defect characteristics. As shown in Figure 18, zone A is located near the center of the gauge section of the test specimens. Zones B is adjacent to zone A, whereas zone C is adjacent to zone B and is located farthest away from the critical section of the test specimen. Zone A is anticipated to experience the largest plastic deformation since it is closest to the critical section. In contrast, zones B and C are expected to undergo relatively less plastic deformation.

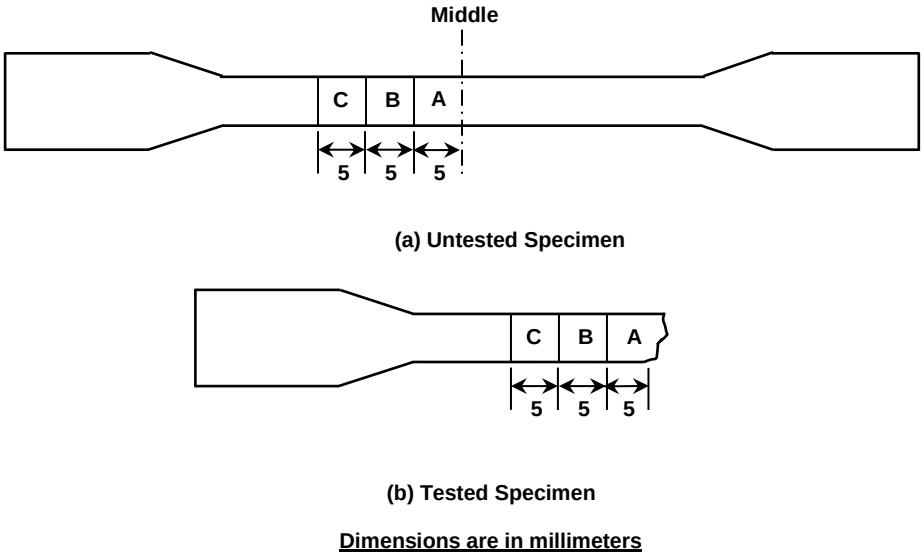

Figure 18. Zones for Micro-CT scan of (a) Untested (b) Tested AM steel specimens.

Defect analysis was performed on the reconstructed 3D image of the steel test specimens using VGStudio Max version 2022.20 (Volume Graphics, Inc.). The features of defects include equivalent spherical diameter, sphericity, number of voids, and void volume fraction. Statistical analysis was conducted for the defect features in the following section.

3. RESULTS AND DISCUSSION

3.1. Growth of the Number of Voids and Void Volume Fraction after Deformation

The present study quantified the change in the number of voids and void volume fraction after deformation in the AM as-built 17-4 stainless steel test specimens. The average void count per cubic millimeter in the three zones (zones A, B, and C) for undeformed specimens RU, CN1, CN2, and CN3 were observed to be 185, 237, 310, and 362, respectively. After the fracture, the average void count per cubic millimeter increased to 299, 390, 794, and 887 in the three zones for specimens RU, CN1, CN2, and CN3, respectively. This implies that the number of voids per cubic millimeter increased by 61.62%, 64.56%, 156.13%, and 145.03% in the three zones after fracture for specimens RU, CN1, CN2, and CN3, respectively (see Figure 19). The increase in the number of voids after fracture indicate void nucleation in the test specimens during the deformation process.

The void volume fraction is a measure of the volume of void per unit volume of material, which is a ratio of the volume of the defects to the total volume of the material in the individual specimen. The average void volume fraction in the three zones of the undeformed specimens RU, CN1, CN2, and CN3 were found to be 2.25%, 3.32%, 3.77%, and 4.19%, respectively. After fracture, the average void volume fractions of the three zones increased to 3.67%, 5.01%, 6.00%, and 6.62% for specimens RU, CN1, CN2, and CN3, respectively. Therefore, the average void volume fractions in the three zones increased by 62.70%, 50.70%, 59.20%, and 57.86% after fracture in specimens RU, CN1, CN2, and CN3, respectively (see Figure 20). The increase in void volume fraction can be attributed to the two phenomena, namely, void nucleation and void growth.

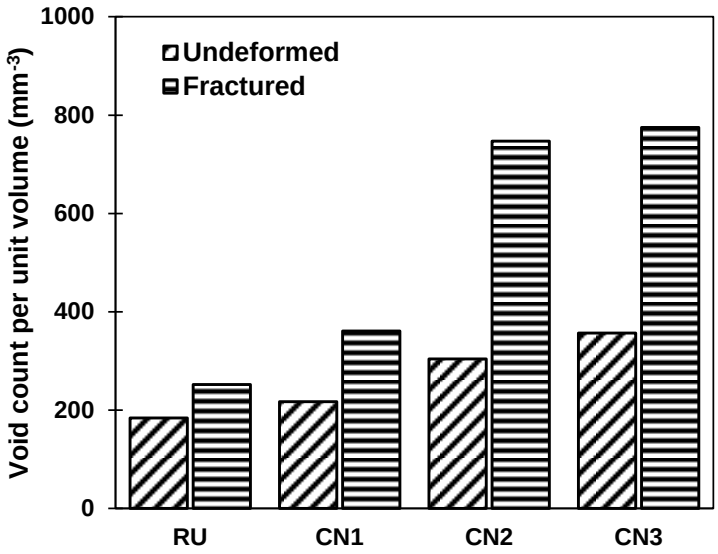

Figure 19. Comparison of average void count per unit volume for undeformed and fractured AM 17-4 steel specimens.

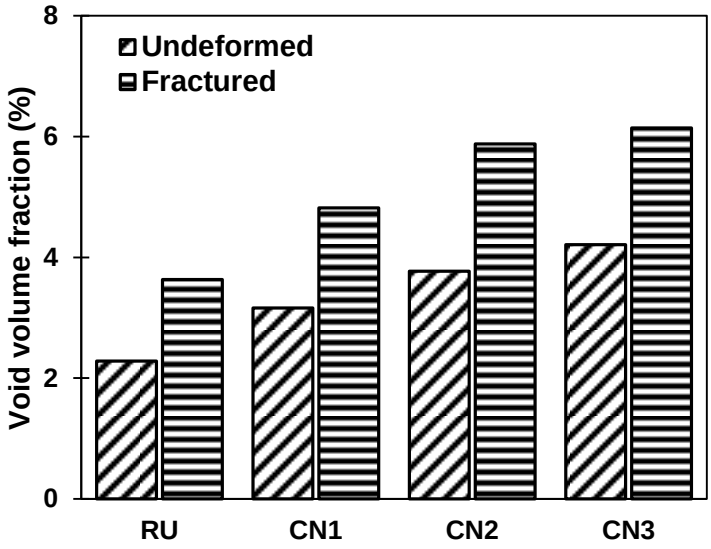

Figure 20. Comparison of average defect volume fraction for undeformed and fractured AM 17-4 steel specimens.

3.2. Statistical Distribution of Void features Before and After Deformation

Statistical analysis of the features of the voids in both undeformed and deformed conditions are presented in this section. Equivalent spherical diameter is a parameter for understanding the defect size present in the test specimens, which is the diameter of a sphere

with an equal defect volume. The equivalent spherical defect diameter distribution for undeformed and deformed zones A, B, and C of the reference unnotched specimen RU are presented in Figure 21. Similarly, the equivalent spherical defect diameter distributions for the zones A, B, and C of the notched specimens CN1, CN2, and CN3 both before and after fracture are presented in Figure 22, Figure 23, and Figure 24, respectively. As evident from the defect equivalent spherical diameter probability density plots, the distributions are asymmetric with the mean defect size being larger than the median, thereby resulting in positively skewed distributions. Based on the statistical analysis of the equivalent spherical defect diameter using probability density plots, the defect sizes present in the notched and unnotched test specimens before and after fracture were observed to follow lognormal distribution. A distribution is considered to be lognormal when the logarithm of the random variable is observed to be follow gaussian distribution and is applicable for non-negative data. Previously, lognormal distribution was used to represent the pore size distribution in metallic and cementitious materials [73,74]. The probability density function of a lognormal distribution is given as

$$y = \frac{1}{x s^* \sqrt{2\pi}} exp\left(\frac{-(logx - \bar{x}^*)^2}{2{s^*}^2}\right), \qquad 0 < x < \infty \tag{1}$$

where, x is the equivalent spherical defect diameter. $\bar{x}^*$ and s^* are two lognormal distribution parameters that denote the mean and standard deviation of the natural logarithm of equivalent spherical defect diameter, respectively. $\bar{x}^*$ and s^* are given as

$$\bar{x}^* = \log(\bar{x}), \quad s^* = \log(s) \tag{2}$$

where, $\bar{x}$ and s are the mean and standard deviation of the equivalent spherical diameter.

More than 98% of the defects present in the unnotched specimen RU and notched specimens CN1, CN2, and CN3 at both undeformed and deformed states were observed to have equivalent spherical defect diameter ranging between 40 μm and 120 μm. Furthermore, the

logarithmic mean ($\bar{x}^*$) of the equivalent spherical defect diameter did not exhibit significant variation before and after fracture in all the three zones for all the unnotched and notched specimens (see Figure 21, Figure 22, Figure 23, and Figure 24). However, the equivalent spherical diameter of the larger defects experienced a substantial change after fracture. For the largest 500 voids in the zone A of the undeformed specimens, the equivalent spherical diameter increased by 11.10%, 7.63%, 2.81%, and 3.11% for specimens RU, CN1, CN2, and CN3, respectively, after the fracture. The equivalent spherical diameter of the largest 200 defects in zone A of the undeformed specimens increased by 13.02%, 8.49%, 5.88%, and 8.77% for the specimens RU, CN1, CN2, and CN3, respectively, after the fracture. Therefore, the significant change in size of the larger defects after fracture indicate that larger defects present in the undeformed specimens dictate the fracture initiation in AM steel. The median, 90th percentile, and 95th percentile equivalent spherical defect diameter in zone A of specimens RU, CN1, CN2, and CN3 for undeformed and deformed conditions are provided in Table 2. In CN1, CN2, and CN3 specimens, the median, 90th percentile, and 95th percentile of equivalent spherical diameter of defects decreased. This can be attributed to higher microvoid nucleation in the notched specimens due to the high stress triaxiality. However, the nucleated voids did not grow significantly due to low fracture strain. The median, 90th percentile, and 95th percentile equivalent spherical defect diameter increased in the RU specimen, which may be attributed to significant growth of the nucleated voids due to higher fracture strain compared to that of the notched specimens.

Table 2. Median, 90th percentile, and 95th percentile equivalent spherical diameter of defects in zone A of undeformed and deformed test specimens.

	Equivalent spherical diameter (µm)							
	RU		**CN1**		**CN2**		**CN3**	
	Undeformed	Deformed	Undeformed	Deformed	Undeformed	Deformed	Undeformed	Deformed
Median	51.71	51.71	53.91	50.53	50.53	45.17	50.53	45.17
90th percentile	77.24	79.74	83.43	78.76	77.75	61.31	75.67	59.63
95th percentile	89.2	94.65	97.32	94.31	92.19	71.71	90.72	69.87

The sphericity distributions of the defects in zones A, B, and C before and after fracture for specimens RU, CN1, CN2, and CN3 are presented in Figure 25, Figure 26, Figure 27, and Figure 28, respectively. The value of sphericity is unity for perfectly spherical defects, whereas highly irregular defects have a sphericity close to zero. In the AM 17-4 stainless specimens, the sphericity of the smaller defects was found to be higher compared to that of the larger defects (see Figure 29). Based on statistical analysis using the probability density plots, the sphericity distributions of the defects present in zones A, B, and C of all the unnotched and notched test specimens before and after fracture were observed to follow the gaussian distribution. The mean sphericity of defects in all the three zones of undeformed RU is 0.57 and after the deformation is 0.56 which represent a slight decrease (see Figure 25). For the CN1 specimen, the mean sphericity of the defects in all the three zones for undeformed and deformed conditions were 0.57 and 0.55, respectively which also showed a slight decrease whereas the standard deviation showed a slight increase in all three zones after fracture (see Figure 26). The mean sphericity of the defects in all the three zones of CN2 and CN3 specimens in the undeformed condition was 0.56 and it slightly increased after fracture to 0.58 whereas, the standard deviation of the sphericity distributions decreased after fracture (see Figure 27 and Figure 28). The newly nucleated voids are smaller in size with higher sphericity. In the case of CN2 and CN3 specimens, the nucleated voids could not get a chance of enough growth due to the lower fracture strain. However, in RU and CN1 specimens, the nucleated voids also dilated or elongated due to higher fracture strains compared to CN2 and CN3 which could reduce the sphericity of the newly nucleated voids.

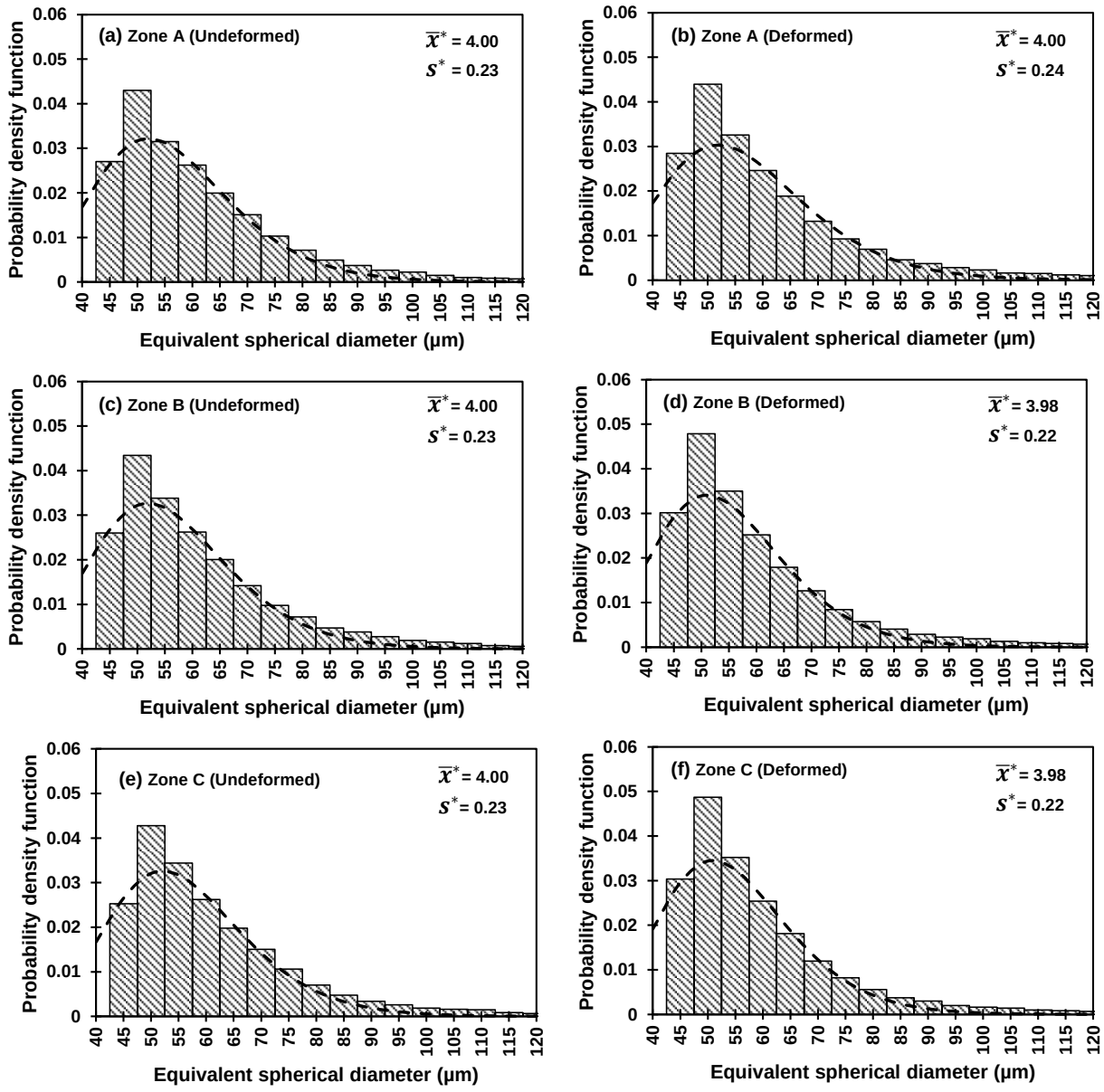

Figure 21. Distribution of equivalent spherical defect diameter of the unnotched specimen. (a) undeformed zone A, (b) deformed zone A, (c) undeformed zone B, (d) deformed zone B, (e) undeformed zone C, and (f) deformed zone C.

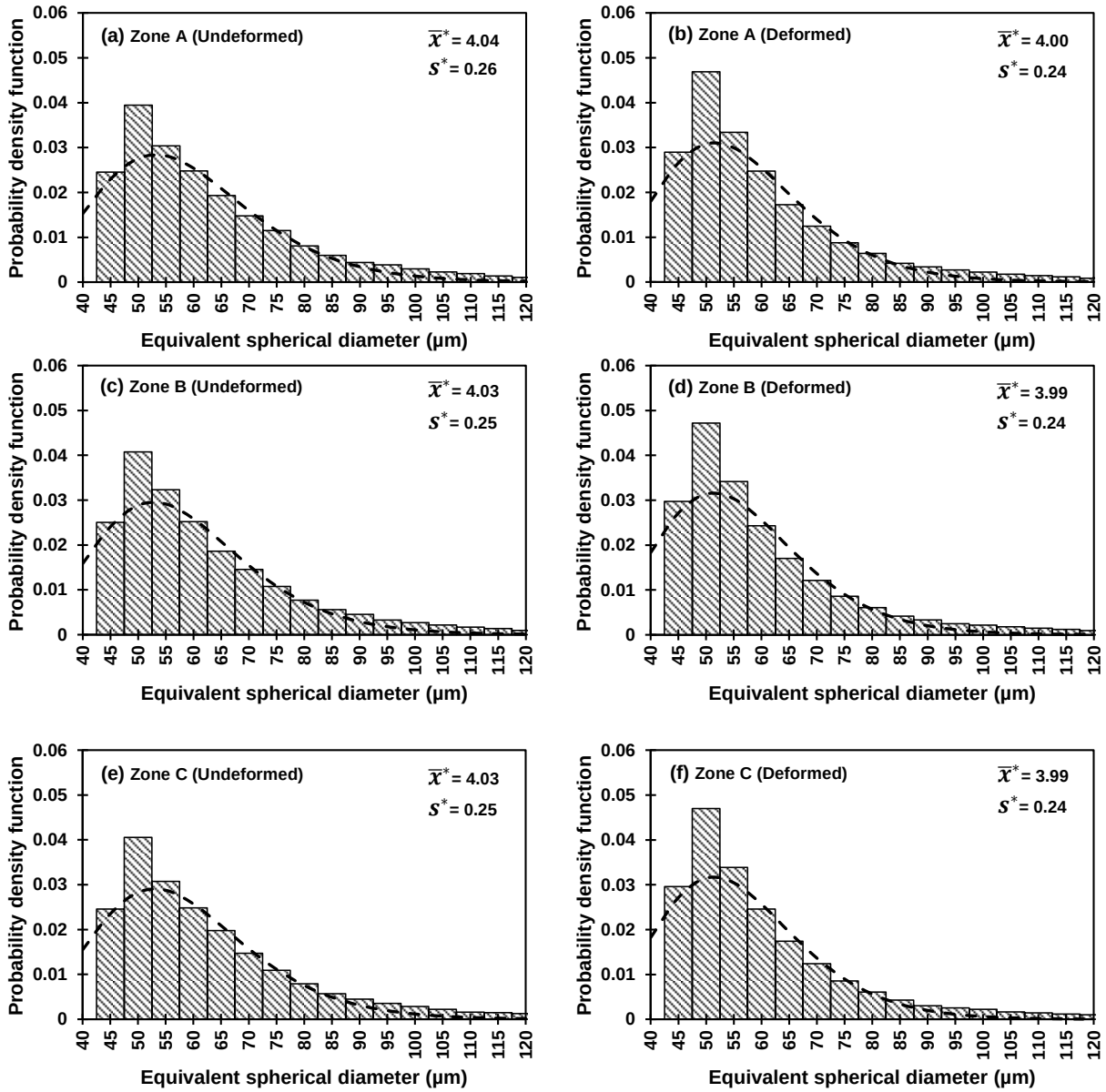

Figure 22. Distribution of equivalent spherical defect diameter of the CN1 specimen. (a) undeformed zone A, (b) deformed zone A, (c) undeformed zone B, (d) deformed zone B, (e) undeformed zone C, and (f) deformed zone C.

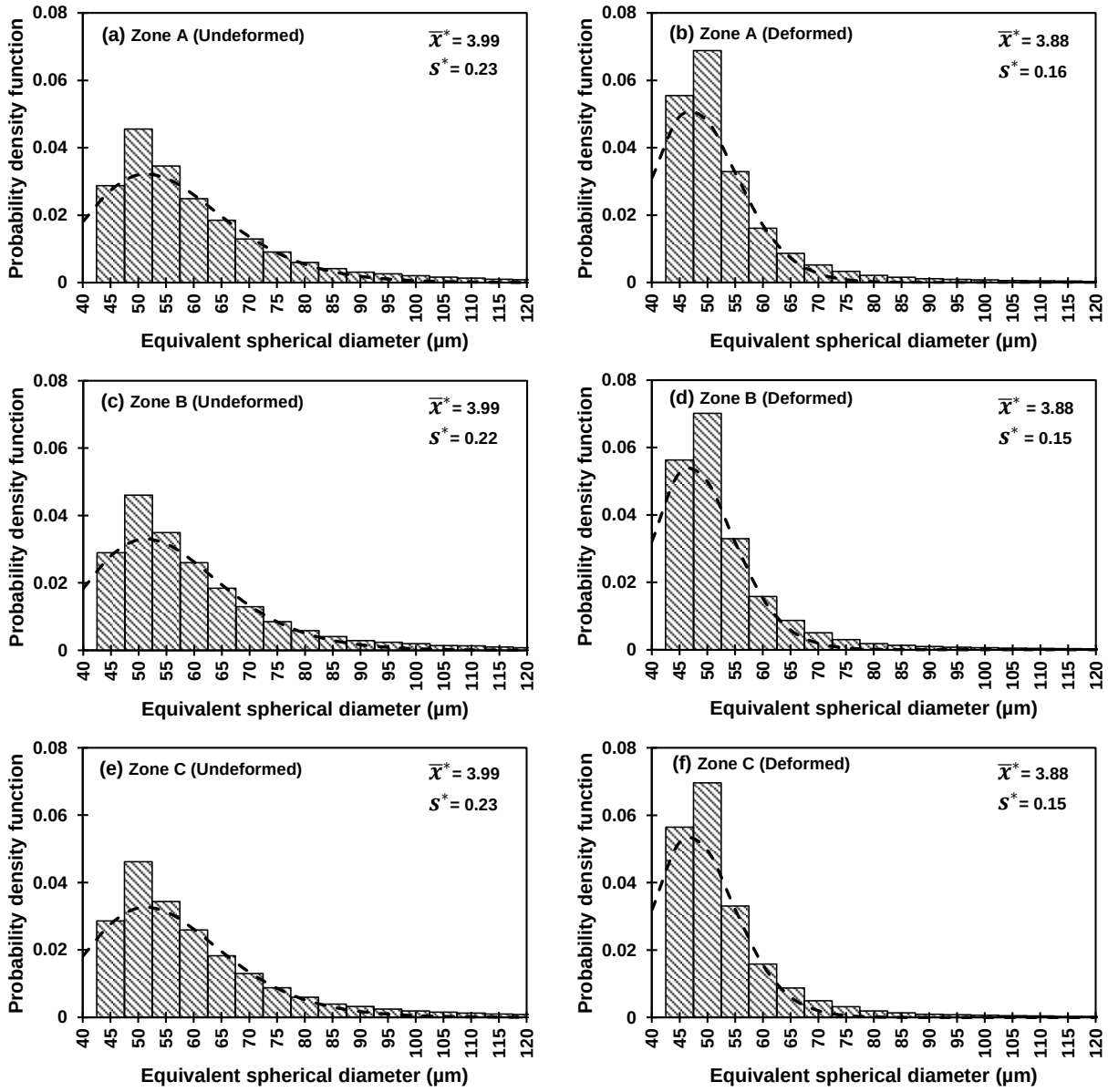

Figure 23. Distribution of equivalent spherical defect diameter of the CN2 specimen. (a) undeformed zone A, (b) deformed zone A, (c) undeformed zone B, (d) deformed zone B, (e) undeformed zone C, and (f) deformed zone C.

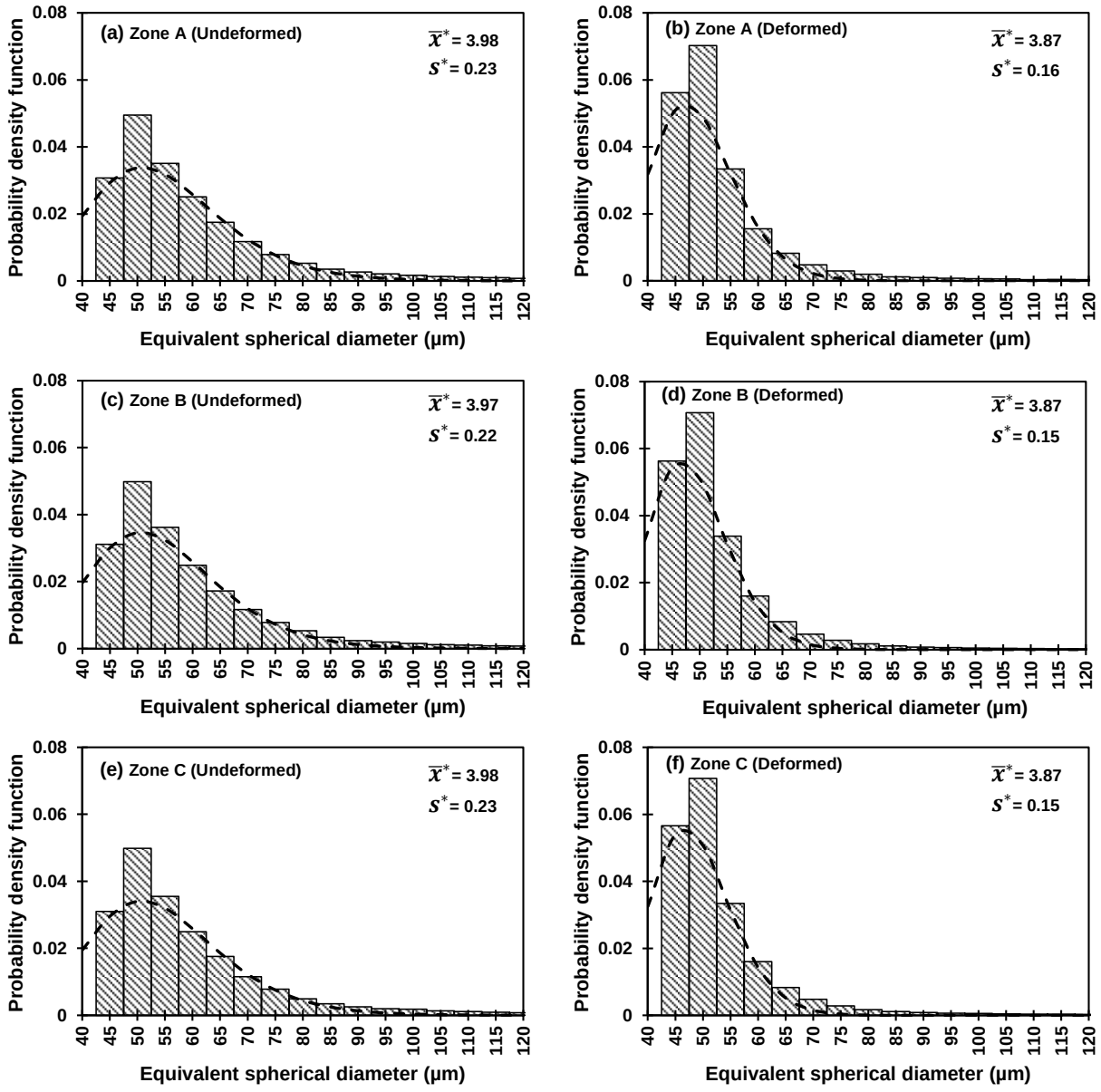

Figure 24. Distribution of equivalent spherical defect diameter of the CN3 specimen. (a) undeformed zone A, (b) deformed zone A, (c) undeformed zone B, (d) deformed zone B, (e) undeformed zone C, and (f) deformed zone C

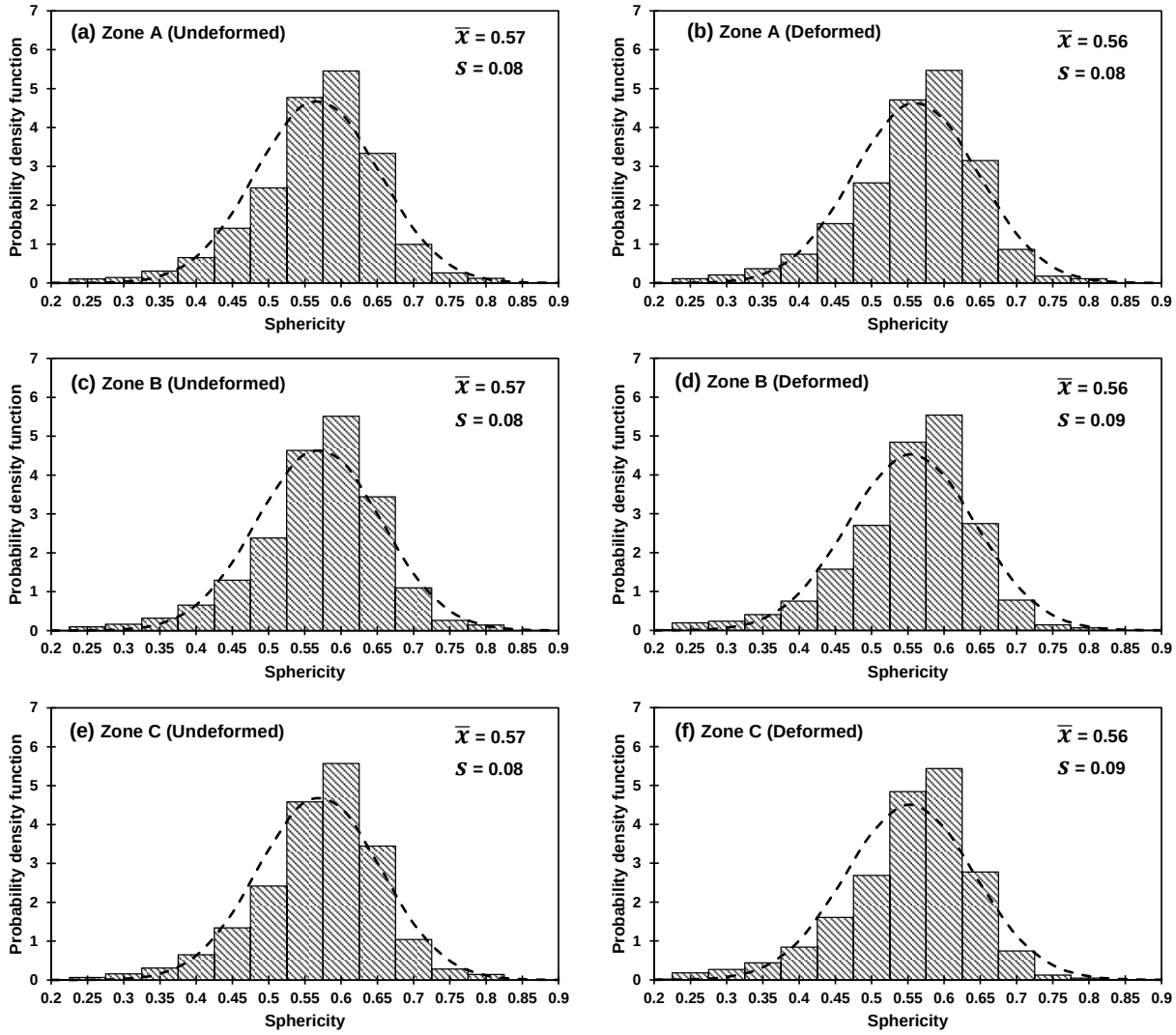

Figure 25. Distribution of sphericity of defects in the unnotched specimen. (a) Undeformed zone A, (b) deformed zone A, (c) undeformed zone B, (d) deformed zone B, (e) undeformed zone C, and (f) deformed zone C.

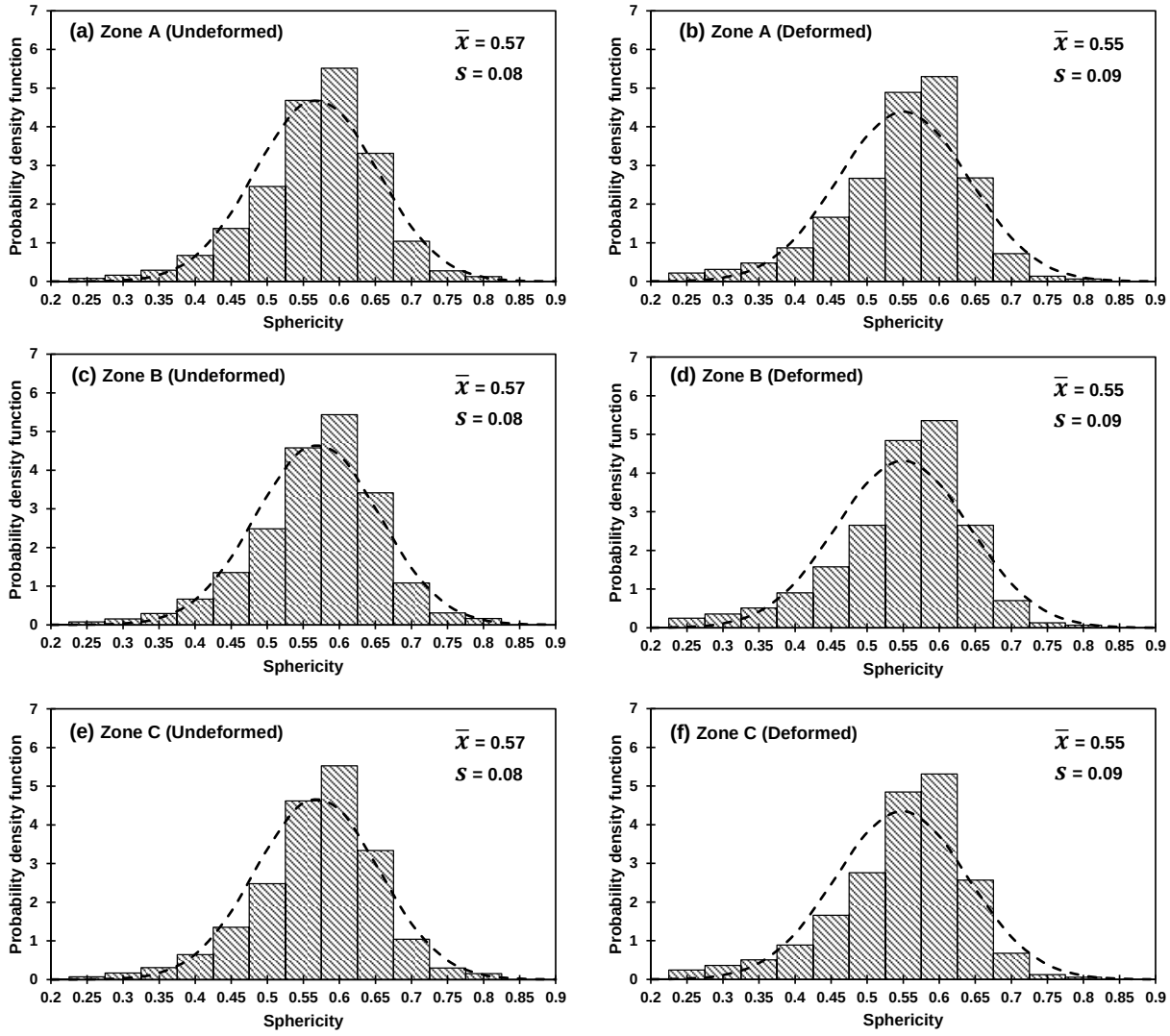

Figure 26. Distribution of sphericity of defects of the CN1 specimen. (a) Undeformed zone A, (b) deformed zone A, (c) undeformed zone B, (d) deformed zone B, (e) undeformed zone C, and (f) deformed zone C.

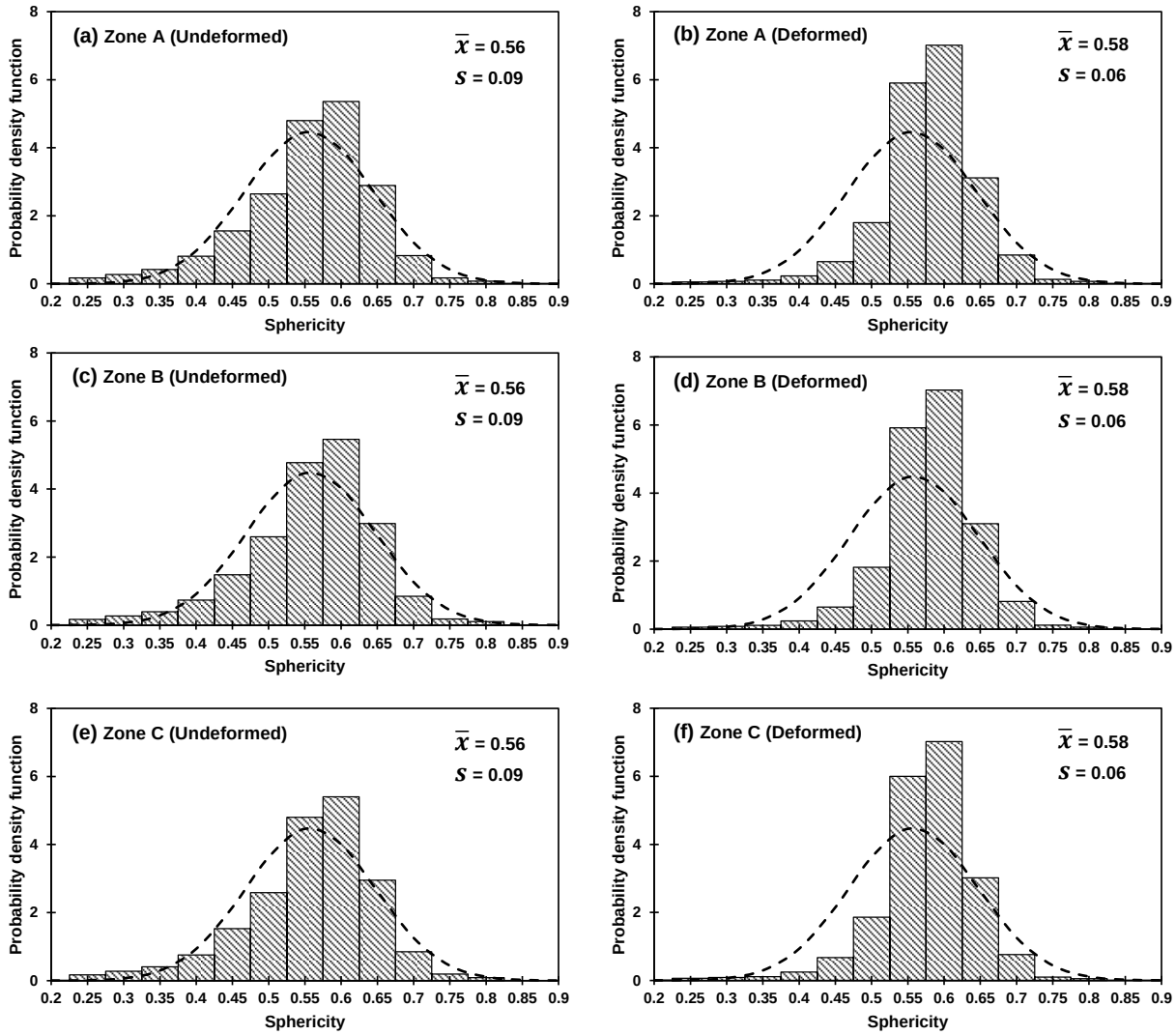

Figure 27. Distribution of sphericity of defects of the CN2 specimen. (a) Undeformed zone A, (b) deformed zone A, (c) undeformed zone B, (d) deformed zone B, (e) undeformed zone C, and (f) deformed zone C.

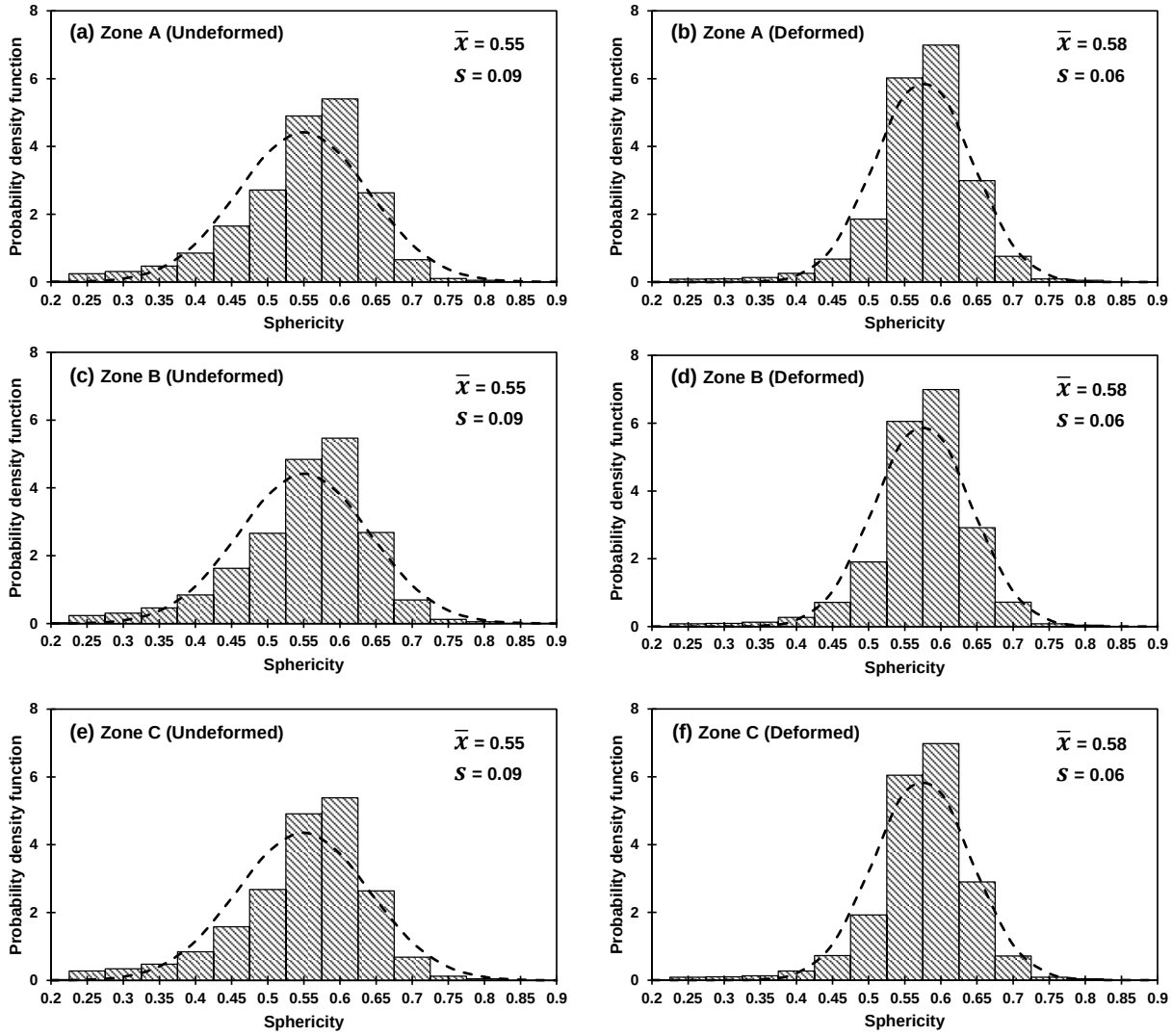

Figure 28. Distribution of sphericity of defects of the CN3 specimen. (a) Undeformed zone A, (b) deformed zone A, (c) undeformed zone B, (d) deformed zone B, (e) undeformed zone C, and (f) deformed zone C.

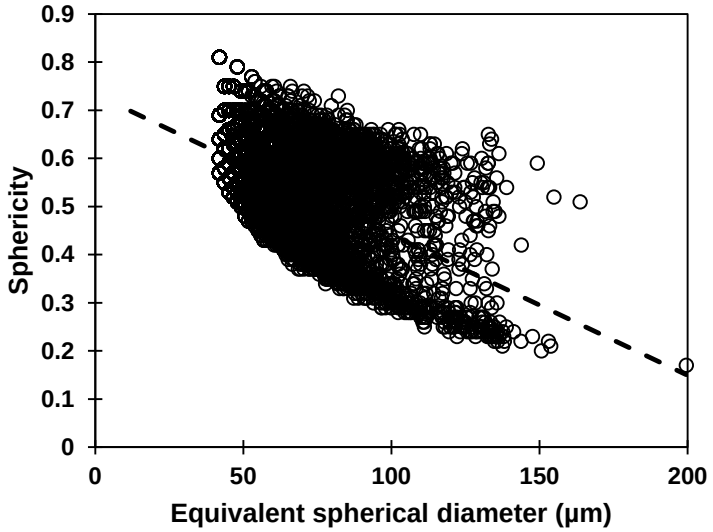

Figure 29. Relationship between sphericity and equivalent spherical diameter for unnotched undeformed AM 17-4 steel specimen.

3.3. Influence of Sudden Geometrical Changes on Size of AM Defects

In the present study, notched specimens were used to investigate the influence of sudden geometric change on the number and density of AM defects. The bar charts providing the void volume fraction in the three zones A, B, and C of all the test specimens is presented in Figure 31. It is important to note that all the three zones in the unnotched specimen RU have a uniform cross-section diameter whereas, Zone A of all the notched specimens have a sudden geometric change unlike the remaining two zones in the notched specimens. As evident from the bar chart presented in Figure 31, the void volume fraction in the three zones of each of the notched specimens are similar after fracture implying that sudden geometric change in AM specimens does not influence the void volume after fracture. However, based on the images extracted using micro-CT, the zone consisting of sudden geometric change (zone A) in all the undeformed notched specimens were found to have larger defects compared to the other zones in the specimen. This can be observed in the defect size (equivalent spherical diameter) distribution

plots where the mean defect size corresponding to zone A in the undeformed notched specimens was higher compared to that of the other zones in the notched specimens. Furthermore, the largest defect size in the undeformed notched specimens was found in zone A of the specimen. The maximum defect size (equivalent spherical diameter) found in zones A, B, and C of undeformed specimen CN1 are 286.52 µm, 172.82 µm, and 164.16 µm, respectively, implying that the largest void present in zone A is ~1.65 times greater than that of the other zones in the specimen. Similar observations were made for undeformed notched specimens CN2 and CN3 where the maximum defect sizes (equivalent spherical diameter) in zone A are 320.41 µm and 386.64 µm which are ~1.68 times and ~2.4 times greater than their counterparts in zones B and C of the undeformed specimens. Therefore, it can be concluded that undeformed as-built AM steel specimens with sudden geometric change such as, notch root of the notched specimens used in this study are prone to larger inherent defects which may result in early fracture initiation in the steel specimens.

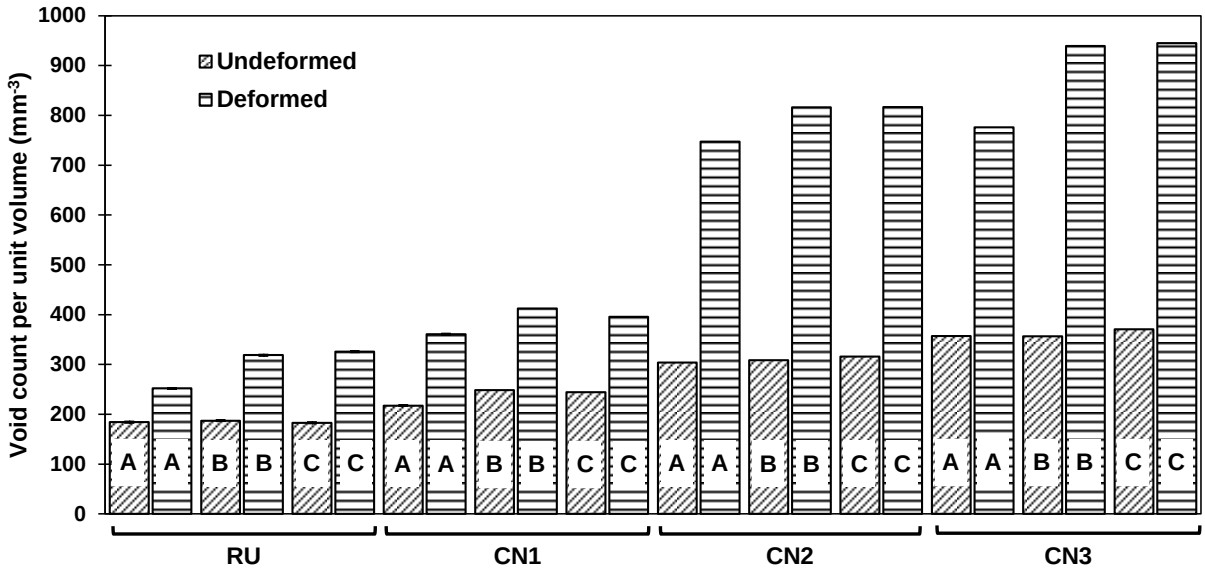

Figure 30. Comparison of the void count per unit volume in undeformed and deformed test specimens.

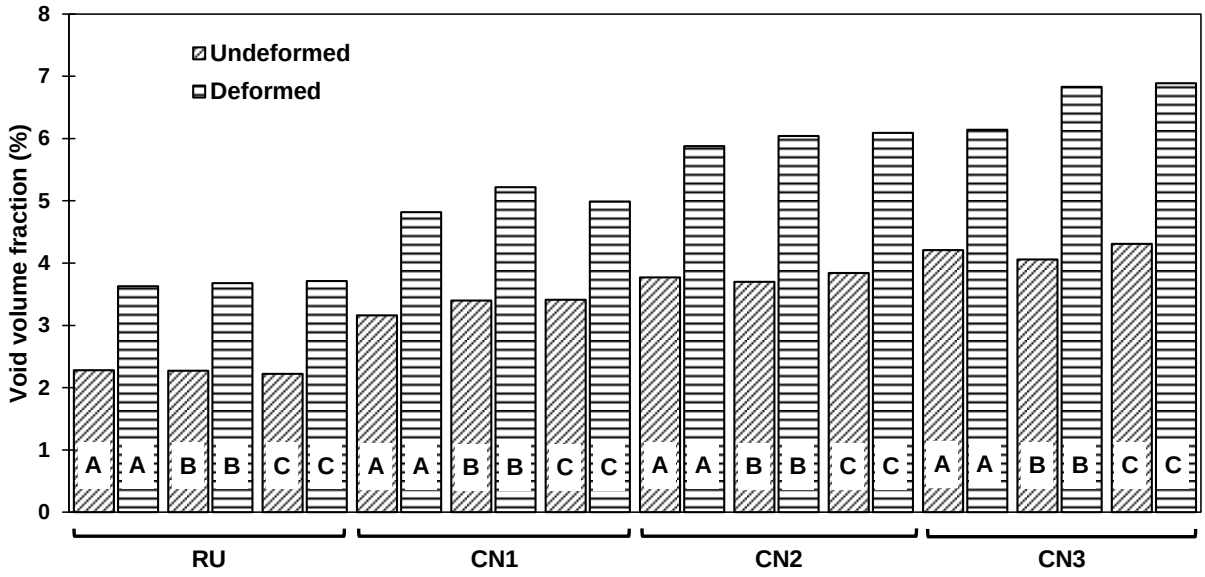

Figure 31. Comparison of the local void volume fraction in undeformed and deformed test specimens.

3.4. Fracture Initiating Mechanism

In the previous sections, the void counts per unit volume and void volume fraction were observed to increase in the deformed test specimens, thereby indicating void nucleation and void growth which are the initial stages of ductile fracture. The increase in void counts per cubic millimeter ranged from ~60% to 145% and the void volume fraction increased by ~50% to 62% in the deformed test specimens. The final stage of ductile fracture involves coalescence of the microvoids present in the specimen over a critical length defined as the characteristic length of the material [75]. The coalesced microvoids were identified using the scanned micro-CT images of the fractured specimens (see Figure *33*). The maximum size of the defects quantified by the equivalent spherical diameter in the deformed specimens are significantly higher than the defects observed in the specimen before fracture (see Figure 32). The maximum equivalent spherical diameter of the defects observed in undeformed specimens RU, CN1, CN2, and CN3 are 199 µm, 286.52 µm, 320.41 µm, and 386.64 µm, respectively whereas, the maximum equivalent

spherical diameter of the coalesced defects in the deformed specimens RU, CN1, CN2, and CN3 are 623.02 µm, 490.71 µm, 391.21 µm, and 538.09 µm, respectively.

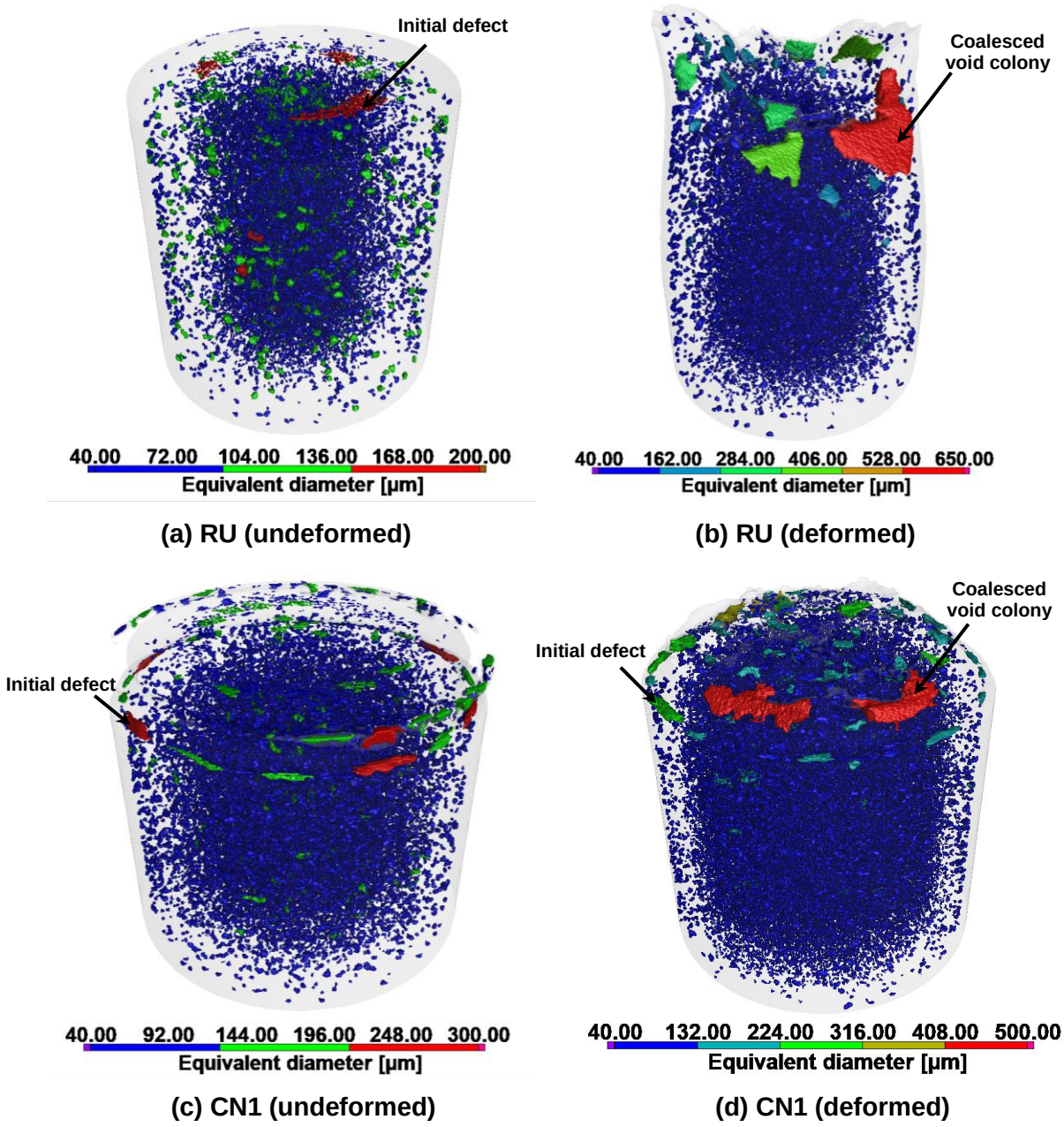

Figure 32. Defects in zone A before and after fracture for specimens (a,b) RU and (c,d) CN1.

Therefore, the coalesced microvoids observed in the micro-CT images and the increase in size of the largest defects observed in the specimens after fracture suggests coalescence of voids

in the test specimens which is the final stage of ductile fracture. The equivalent spherical diameter of these coalesced voids range between 350-600 μm suggesting that the voids coalesce over this critical length to initiate ductile fracture in AM steel specimens. Therefore, the increase in the number of voids, void volume fraction, and the presence of coalesced microvoids in the fractured specimens provide sufficient evidence of ductile fracture in the as-built AM steel test specimens which is not apparent in the SEM analysis.

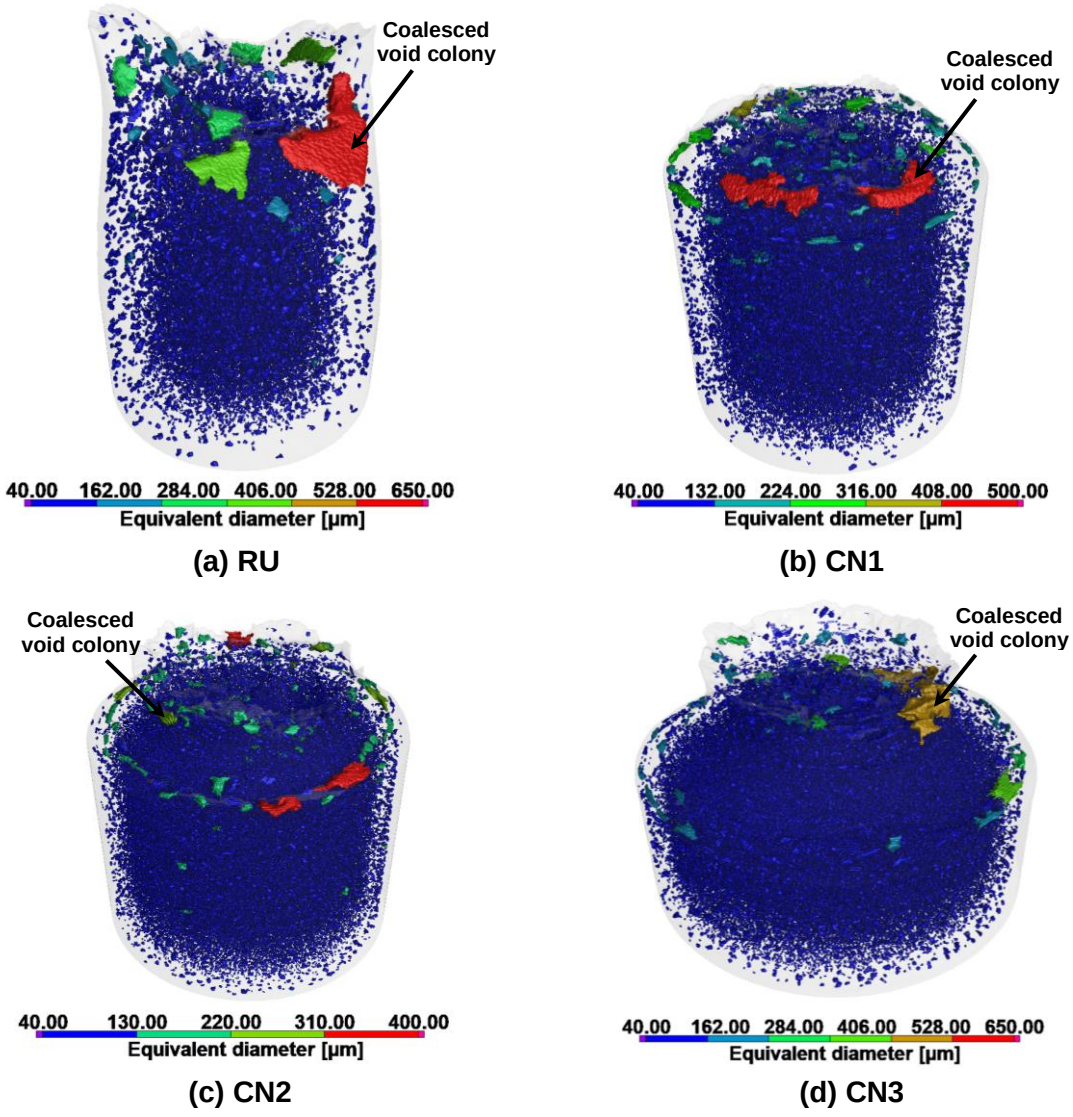

Figure 33. Defects in zone A of deformed test specimens (a) RU, (b) CN1, (c) CN2, and (d) CN3.

4. CONCLUSIONS, IMPLICATIONS, AND FUTURE RECOMMENDATIONS

4.1. Conclusions

The following important conclusions can be made from this study

1. The number of voids per cubic millimeter increased by 61.62%, 64.56%, 156.13%, and 145.03% after fracture in specimens RU, CN1, CN2, and CN3, respectively which provides evidence of void nucleation in the test specimens.
2. The void volume fraction increased by 59%, 52%, 55%, and 45% for specimens RU, CN1, CN2, and CN3 which can be attributed to void nucleation and subsequent void growth in the specimens.
3. Larger defects have significantly higher growth during deformation. Top 500 defects have an increment of 2-11% and for the top 200 defects an increment of 5-13% for the specimens.
4. Geometrical intricacy can result in inherent large defects in the AM components. Large defects were observed in the notch root and the equivalent spherical diameters in zone A is ~1.65-2.4 times greater than their counterparts in zones B and C of the undeformed notched specimens which can be attributed to the sudden change in geometry of the test specimens.
5. Coalesced defects with equivalent spherical diameters of 623 μm, 490 μm, 354 μm, and 538 μm are found in the deformed specimens RU, CN1, CN2, and CN3, respectively. This provides evidence of void coalescence in the AM 17-4 steel specimens.
6. The micro-CT analysis provided evidence of microvoid nucleation (61-156% increase), dilation (45-59% volume change including the newly nucleated voids) and coalescence over a length varying between 350-623 microns in the AM 17-4 steel indicating that the

ductile fracture to be the fracture initiating mechanism. The characteristic length for the damage in the AM steel is around 600 μm.

4.2. Practical Implications of Current Research and Future Recommendations

1. The current study reveals the defect distributions and their effects on the fracture, which can provide a deeper understanding of controlling the AM defects to delay fracture initiation and improve the performance of the AM steels. Since the fracture initiation in the AM 17-4 stainless steel is significantly influenced by the existence of larger defects, future additive manufacturing efforts should focus on controlling the larger defects in AM parts.
2. Geometrical intricacies introduce larger defects, which could be detrimental to the AM components. Thus, appropriate process and build parameters should be considered for AM components to produce geometrically intricate components.
3. This study revealed the effects of the inherent defects in the ductile fracture initiation of the AM steel. More efforts should be given to determine the effects of the metallurgical heterogeneity, anisotropy, and residual stress on the ductile fracture initiation.
4. Post-treatment in AM components can potentially reduce the inherent defects in AM steels. This study should be repeated for the heat-treated AM steels to investigate their fracture-initiating mechanisms.
5. This study is limited to defect characterization before and after fracture in AM specimens. The same statistical study can be conducted in several loading intervals to characterize the dilation and elongation of the nucleated and inherent defects.
6. The existing uncoupled and coupled ductile fracture models can be modified by incorporating this study's statistical understanding of the defect size distribution and growth to predict fracture initiation in AM components.

REFERENCES

[1] Frazier WE. Metal Additive Manufacturing: A Review. J of Materi Eng and Perform 2014;23:1917–28. https://doi.org/10.1007/s11665-014-0958-z.

[2] Bajaj P, Hariharan A, Kini A, Kürnsteiner P, Raabe D, Jägle EA. Steels in additive manufacturing: A review of their microstructure and properties. Materials Science and Engineering: A 2020;772:138633. https://doi.org/10.1016/j.msea.2019.138633.

[3] Ahn D-G. Direct metal additive manufacturing processes and their sustainable applications for green technology: A review. Int J of Precis Eng and Manuf-Green Tech 2016;3:381–95. https://doi.org/10.1007/s40684-016-0048-9.

[4] Meng LX, Ben DD, Yang HJ, Ji HB, Lian DL, Zhu YK, et al. Effects of embedded spherical pore on the tensile properties of a selective laser melted Ti6Al4V alloy. Materials Science and Engineering: A 2021;815:141254. https://doi.org/10.1016/j.msea.2021.141254.

[5] DebRoy T, Wei HL, Zuback JS, Mukherjee T, Elmer JW, Milewski JO, et al. Additive manufacturing of metallic components – Process, structure and properties. Progress in Materials Science 2018;92:112–224. https://doi.org/10.1016/j.pmatsci.2017.10.001.

[6] Herzog D, Seyda V, Wycisk E, Emmelmann C. Additive manufacturing of metals. Acta Materialia 2016;117:371–92. https://doi.org/10.1016/j.actamat.2016.07.019.

[7] Ghods S, Schur R, Schultz E, Pahuja R, Montelione A, Wisdom C, et al. Powder reuse and its contribution to porosity in additive manufacturing of Ti6Al4V. Materialia 2021;15:100992. https://doi.org/10.1016/j.mtla.2020.100992.

[8] King WE, Anderson AT, Ferencz RM, Hodge NE, Kamath C, Khairallah SA, et al. Laser powder bed fusion additive manufacturing of metals; physics, computational, and

materials challenges. Applied Physics Reviews 2015;2:041304. https://doi.org/10.1063/1.4937809.

[9] Ahmed N, Barsoum I, Haidemenopoulos G, Al-Rub RKA. Process parameter selection and optimization of laser powder bed fusion for 316L stainless steel: A review. Journal of Manufacturing Processes 2022;75:415–34. https://doi.org/10.1016/j.jmapro.2021.12.064.

[10] Shapiro AA, Borgonia JP, Chen QN, Dillon RP, McEnerney B, Polit-Casillas R, et al. Additive Manufacturing for Aerospace Flight Applications. Journal of Spacecraft and Rockets 2016;53:952–9. https://doi.org/10.2514/1.A33544.

[11] Snyder JC, Thole KA. Effect of Additive Manufacturing Process Parameters on Turbine Cooling. Journal of Turbomachinery 2020;142:051007. https://doi.org/10.1115/1.4046459.

[12] Saltzman D, Bichnevicius M, Lynch S, Simpson TW, Reutzel EW, Dickman C, et al. Design and evaluation of an additively manufactured aircraft heat exchanger. Applied Thermal Engineering 2018;138:254–63. https://doi.org/10.1016/j.applthermaleng.2018.04.032.

[13] Kerstens F, Cervone A, Gradl P. End to end process evaluation for additively manufactured liquid rocket engine thrust chambers. Acta Astronautica 2021;182:454–65. https://doi.org/10.1016/j.actaastro.2021.02.034.

[14] Ford S, Despeisse M. Additive manufacturing and sustainability: an exploratory study of the advantages and challenges. Journal of Cleaner Production 2016;137:1573–87. https://doi.org/10.1016/j.jclepro.2016.04.150.

[15] Tomlin M, Meyer J. Topology Optimization of an Additive Layer Manufactured (ALM) Aerospace Part 2011:9.

[16] Gradl PR, Greene SE, Protz C, Bullard B, Buzzell J, Garcia C, et al. Additive Manufacturing of Liquid Rocket Engine Combustion Devices: A Summary of Process Developments and Hot-Fire Testing Results. 2018 Joint Propulsion Conference, Cincinnati, Ohio: American Institute of Aeronautics and Astronautics; 2018. https://doi.org/10.2514/6.2018-4625.

[17] Sun C, Wang Y, McMurtrey MD, Jerred ND, Liou F, Li J. Additive manufacturing for energy: A review. Applied Energy 2021;282:116041. https://doi.org/10.1016/j.apenergy.2020.116041.

[18] Pikul JH, Gang Zhang H, Cho J, Braun PV, King WP. High-power lithium ion microbatteries from interdigitated three-dimensional bicontinuous nanoporous electrodes. Nat Commun 2013;4:1732. https://doi.org/10.1038/ncomms2747.

[19] You J, Preen RJ, Bull L, Greenman J, Ieropoulos I. 3D printed components of microbial fuel cells: Towards monolithic microbial fuel cell fabrication using additive layer manufacturing. Sustainable Energy Technologies and Assessments 2017;19:94–101. https://doi.org/10.1016/j.seta.2016.11.006.

[20] Kumar R, Kumar M, Chohan JS. The role of additive manufacturing for biomedical applications: A critical review. Journal of Manufacturing Processes 2021;64:828–50. https://doi.org/10.1016/j.jmapro.2021.02.022.

[21] du Plessis A, Yadroitsava I, Yadroitsev I. Effects of defects on mechanical properties in metal additive manufacturing: A review focusing on X-ray tomography insights. Materials & Design 2020;187:108385. https://doi.org/10.1016/j.matdes.2019.108385.

[22] Sanaei N, Fatemi A, Phan N. Defect characteristics and analysis of their variability in metal L-PBF additive manufacturing. Materials & Design 2019;182:108091. https://doi.org/10.1016/j.matdes.2019.108091.

[23] Dennies DP. Critical Thinking in the Application of Additive Manufacturing Processes: A Review. J Fail Anal and Preven 2021;21:1099–125. https://doi.org/10.1007/s11668-021-01175-x.

[24] Torries B, Imandoust A, Beretta S, Shao S, Shamsaei N. Overview on Microstructure- and Defect-Sensitive Fatigue Modeling of Additively Manufactured Materials. JOM 2018;70:1853–62. https://doi.org/10.1007/s11837-018-2987-9.

[25] Gorsse S, Hutchinson C, Gouné M, Banerjee R. Additive manufacturing of metals: a brief review of the characteristic microstructures and properties of steels, Ti-6Al-4V and high-entropy alloys. Science and Technology of Advanced Materials 2017;18:584–610. https://doi.org/10.1080/14686996.2017.1361305.

[26] Hales C, Pattin C. Design Review for Failure Analysis and Prevention 2002. https://doi.org/10.31399/asm.hb.v11.a0003502.

[27] Mostafaei A, Zhao C, He Y, Reza Ghiaasiaan S, Shi B, Shao S, et al. Defects and anomalies in powder bed fusion metal additive manufacturing. Current Opinion in Solid State and Materials Science 2022;26:100974. https://doi.org/10.1016/j.cossms.2021.100974.

[28] Zhu HH, Fuh JYH, Lu L. The influence of powder apparent density on the density in direct laser-sintered metallic parts. International Journal of Machine Tools and Manufacture 2007;47:294–8. https://doi.org/10.1016/j.ijmachtools.2006.03.019.

[29] Singla AK, Banerjee M, Sharma A, Singh J, Bansal A, Gupta MK, et al. Selective laser melting of Ti6Al4V alloy: Process parameters, defects and post-treatments. Journal of Manufacturing Processes 2021;64:161–87. https://doi.org/10.1016/j.jmapro.2021.01.009.

[30] Sanaei N, Fatemi A. Defects in additive manufactured metals and their effect on fatigue performance: A state-of-the-art review. Progress in Materials Science 2021;117:100724. https://doi.org/10.1016/j.pmatsci.2020.100724.

[31] Xu W, Brandt M, Sun S, Elambasseril J, Liu Q, Latham K, et al. Additive manufacturing of strong and ductile Ti–6Al–4V by selective laser melting via in situ martensite decomposition. Acta Materialia 2015;85:74–84. https://doi.org/10.1016/j.actamat.2014.11.028.

[32] Gong H, Rafi K, Gu H, Janaki Ram GD, Starr T, Stucker B. Influence of defects on mechanical properties of Ti–6Al–4V components produced by selective laser melting and electron beam melting. Materials & Design 2015;86:545–54. https://doi.org/10.1016/j.matdes.2015.07.147.

[33] Shao S, Mahtabi MJ, Shamsaei N, Thompson SM. Solubility of argon in laser additive manufactured α-titanium under hot isostatic pressing condition. Computational Materials Science 2017;131:209–19. https://doi.org/10.1016/j.commatsci.2017.01.040.

[34] Dilip JJS, Zhang S, Teng C, Zeng K, Robinson C, Pal D, et al. Influence of processing parameters on the evolution of melt pool, porosity, and microstructures in Ti-6Al-4V alloy parts fabricated by selective laser melting. Prog Addit Manuf 2017;2:157–67. https://doi.org/10.1007/s40964-017-0030-2.

[35] Sun Y, Hebert RJ, Aindow M. Effect of heat treatments on microstructural evolution of additively manufactured and wrought 17-4PH stainless steel. Materials & Design 2018;156:429–40. https://doi.org/10.1016/j.matdes.2018.07.015.

[36] Tammas-Williams S, Withers PJ, Todd I, Prangnell PB. The Effectiveness of Hot Isostatic Pressing for Closing Porosity in Titanium Parts Manufactured by Selective Electron Beam Melting. Metall Mater Trans A 2016;47:1939–46. https://doi.org/10.1007/s11661-016-3429-3.

[37] Tammas-Williams S, Withers PJ, Todd I, Prangnell PB. Porosity regrowth during heat treatment of hot isostatically pressed additively manufactured titanium components. Scripta Materialia 2016;122:72–6. https://doi.org/10.1016/j.scriptamat.2016.05.002.

[38] Wits WW, Carmignato S, Zanini F, Vaneker THJ. Porosity testing methods for the quality assessment of selective laser melted parts. CIRP Annals 2016;65:201–4. https://doi.org/10.1016/j.cirp.2016.04.054.

[39] Elmoutaouakkil A, Salvo L, Maire E, Peix G. 2D and 3D Characterization of Metal Foams Using X-ray Tomography. Advanced Engineering Materials 2002;4:803–7. https://doi.org/10.1002/1527-2648(20021014)4:10<803::AID-ADEM803>3.0.CO;2-D.

[40] Solberg K, Guan S, Razavi SMJ, Welo T, Chan KC, Berto F. Fatigue of additively manufactured 316L stainless steel: The influence of porosity and surface roughness. Fatigue & Fracture of Engineering Materials & Structures 2019;42:2043–52. https://doi.org/10.1111/ffe.13077.

[41] Gong H, Nadimpalli VK, Rafi K, Starr T, Stucker B. Micro-CT Evaluation of Defects in Ti-6Al-4V Parts Fabricated by Metal Additive Manufacturing. Technologies 2019;7:44. https://doi.org/10.3390/technologies7020044.

[42] Wilson-Heid AE, Novak TC, Beese AM. Characterization of the Effects of Internal Pores on Tensile Properties of Additively Manufactured Austenitic Stainless Steel 316L. Exp Mech 2019;59:793–804. https://doi.org/10.1007/s11340-018-00465-0.

[43] Berez J, Sheridan L, Saldaña C. Extreme variation in fatigue: Fatigue life prediction and dependence on build volume location in laser powder bed fusion of 17-4 stainless steel. International Journal of Fatigue 2022;158:106737. https://doi.org/10.1016/j.ijfatigue.2022.106737.

[44] Pineau A, Benzerga AA, Pardoen T. Failure of metals I: Brittle and ductile fracture. Acta Materialia 2016;107:424–83. https://doi.org/10.1016/j.actamat.2015.12.034.

[45] Besson J. Continuum models of ductile fracture : A review. International Journal of Damage Mechanics 2010;19:3–52. https://doi.org/10.1177/1056789509103482.

[46] Yang X, Li Y, Jiang W, Duan M, Chen D, Li B. Ductile fracture prediction of additive manufactured Ti6Al4V alloy based on an extended GTN damage model. Engineering Fracture Mechanics 2021;256:107989. https://doi.org/10.1016/j.engfracmech.2021.107989.

[47] Muro-Barrios R, Cui Y, Lambros J, Chew HB. Dual-scale porosity effects on crack growth in additively manufactured metals: 3D ductile fracture models. Journal of the Mechanics and Physics of Solids 2022;159:104727. https://doi.org/10.1016/j.jmps.2021.104727.

[48] Nalli F, Cortese L, Concli F. Ductile damage assessment of Ti6Al4V, 17-4PH and AlSi10Mg for additive manufacturing. Engineering Fracture Mechanics 2021;241:107395. https://doi.org/10.1016/j.engfracmech.2020.107395.

[49] Naragani DP, Park J-S, Kenesei P, Sangid MD. Void coalescence and ductile failure in IN718 investigated via high-energy synchrotron X-ray tomography and diffraction. Journal of the Mechanics and Physics of Solids 2020;145:104155. https://doi.org/10.1016/j.jmps.2020.104155.

[50] Kim FH, Moylan SP, Phan TQ, Garboczi EJ. Investigation of the Effect of Artificial Internal Defects on the Tensile Behavior of Laser Powder Bed Fusion 17–4 Stainless Steel Samples: Simultaneous Tensile Testing and X-Ray Computed Tomography. Exp Mech 2020;60:987–1004. https://doi.org/10.1007/s11340-020-00604-6.

[51] Miers JC, Moore DG, Saldana C. Defect Evolution in Tensile Loading of 316L Processed by Laser Powder Bed Fusion. Exp Mech 2022;62:969–83. https://doi.org/10.1007/s11340-021-00815-5.

[52] Singh R, Rishab, Sidhu JS. On three-dimensional printing of 17-4 precipitation-hardenable stainless steel with direct metal laser sintering in aircraft structural applications. Proceedings of the Institution of Mechanical Engineers, Part L: Journal of Materials: Design and Applications 2022;236:440–50. https://doi.org/10.1177/14644207211044804.

[53] Soja A, Li J, Tredinnick S, Woodfield T. Surface finishing of additively manufactured stainless steel surgical instruments. Rapid Prototyping Journal 2020;27:59–70. https://doi.org/10.1108/RPJ-01-2020-0009.

[54] Huang L, Cao Y, Zhao H, Li Y, Wang Y, Wei L. Effect of process parameters on density and mechanical behaviour of a selective laser melted 17-4PH stainless steel alloy. Open Physics 2022;20:66–77. https://doi.org/10.1515/phys-2022-0008.

[55] Bai B, Hu R, Zhang C, Xue J, Yang W. Effect of precipitates on hardening of 17-4PH martensitic stainless steel serviced at 300 °C in nuclear power plant. Annals of Nuclear Energy 2021;154:108123. https://doi.org/10.1016/j.anucene.2020.108123.

[56] Jiang T, Zhong J, Zhang X, Wang W, Guan K. Hydrogen embrittlement induced fracture of 17-4 PH stainless steel valve stem. Engineering Failure Analysis 2020;113:104576. https://doi.org/10.1016/j.engfailanal.2020.104576.

[57] Avner SH. Introduction to Physical Metallurgy. McGraw-Hill; 1974.

[58] Ye D, Li J, Jiang W, Su J, Zhao K. Effect of Cu addition on microstructure and mechanical properties of 15%Cr super martensitic stainless steel. Materials & Design 2012;41:16–22. https://doi.org/10.1016/j.matdes.2012.04.036.

[59] Wu J-H, Lin C-K. Tensile and fatigue properties of 17-4 PH stainless steel at high temperatures. Metall Mater Trans A 2002;33:1715–24. https://doi.org/10.1007/s11661-002-0180-8.

[60] Suri P, Smarslok BP, German RM. Impact properties of sintered and wrought 17–4 PH stainless steel. Powder Metallurgy 2006;49:40–7. https://doi.org/10.1179/174329006X89317.

[61] Alnajjar M, Christien F, Bosch C, Wolski K. A comparative study of microstructure and hydrogen embrittlement of selective laser melted and wrought 17–4 PH stainless steel. Materials Science and Engineering: A 2020;785:139363. https://doi.org/10.1016/j.msea.2020.139363.

[62] Zaefferer S, Elhami N-N, Konijnenberg P. 18 - Electron backscatter diffraction (EBSD) techniques for studying phase transformations in steels. In: Pereloma E, Edmonds DV,

editors. Phase Transformations in Steels, vol. 2, Woodhead Publishing; 2012, p. 557–87. https://doi.org/10.1533/9780857096111.4.557.

[63] Akhtar K, Khan SA, Khan SB, Asiri AM. Scanning Electron Microscopy: Principle and Applications in Nanomaterials Characterization. In: Sharma SK, editor. Handbook of Materials Characterization, Cham: Springer International Publishing; 2018, p. 113–45. https://doi.org/10.1007/978-3-319-92955-2_4.

[64] Goldstein JI, Newbury DE, Echlin P, Joy DC, Romig AD, Lyman CE, et al. Scanning Electron Microscopy and X-Ray Microanalysis: A Text for Biologists, Materials Scientists, and Geologists. Boston, MA: Springer US; 1992. https://doi.org/10.1007/978-1-4613-0491-3.

[65] Evans CA, Novak SW. Microelectronics Processing: Inorganic Materials Characterization Edited by Lawrence Casper. MRS Bulletin 1987;12:106–106. https://doi.org/10.1557/S0883769400067373.

[66] Reimschuessel AC. Scanning electron microscopy - Part I. J Chem Educ 1972;49:A413. https://doi.org/10.1021/ed049pA413.

[67] Orhan K, editor. Micro-computed Tomography (micro-CT) in Medicine and Engineering. Cham: Springer International Publishing; 2020. https://doi.org/10.1007/978-3-030-16641-0.

[68] Vásárhelyi L, Kónya Z, Kukovecz Á, Vajtai R. Microcomputed tomography–based characterization of advanced materials: a review. Materials Today Advances 2020;8:100084. https://doi.org/10.1016/j.mtadv.2020.100084.

[69] Barigou M, Douaire M. 9 - X-ray micro-computed tomography for resolving food microstructures. In: Morris VJ, Groves K, editors. Food Microstructures, Woodhead Publishing; 2013, p. 246–72. https://doi.org/10.1533/9780857098894.1.246.

[70] Kiran R, Khandelwal K. Experimental Studies and Models for Ductile Fracture in ASTM A992 Steels at High Triaxiality. Journal of Structural Engineering 2014;140:04013044. https://doi.org/10.1061/(ASCE)ST.1943-541X.0000828.

[71] Kuwamura H, Yamamoto K. Ductile Crack as Trigger of Brittle Fracture in Steel. Journal of Structural Engineering 1997;123:729–35. https://doi.org/10.1061/(ASCE)0733-9445(1997)123:6(729).

[72] Jost EW, Miers JC, Robbins A, Moore DG, Saldana C. Effects of spatial energy distribution-induced porosity on mechanical properties of laser powder bed fusion 316L stainless steel. Additive Manufacturing 2021;39:101875. https://doi.org/10.1016/j.addma.2021.101875.

[73] Eliaz N, Foucks N, Geva D, Oren S, Shriki N, Vaknin D, et al. Comparative Quality Control of Titanium Alloy Ti–6Al–4V, 17–4 PH Stainless Steel, and Aluminum Alloy 4047 Either Manufactured or Repaired by Laser Engineered Net Shaping (LENS). Materials 2020;13:4171. https://doi.org/10.3390/ma13184171.

[74] Kim KY, Yun TS, Choo J, Kang DH, Shin HS. Determination of air-void parameters of hardened cement-based materials using X-ray computed tomography. Construction and Building Materials 2012;37:93–101. https://doi.org/10.1016/j.conbuildmat.2012.07.012.

[75] Lou Y, Yoon JW, Huh H, Chao Q, Song J-H. Correlation of the maximum shear stress with micro-mechanisms of ductile fracture for metals with high strength-to-weight ratio.

International Journal of Mechanical Sciences 2018;146–147:583–601. https://doi.org/10.1016/j.ijmecsci.2018.03.025.